Applied Physics A (2022) 128:1018
https://doi.org/10.1007/s00339-022-06154-z

Applied Physics A
Materials Science & Processing

Efficient preparation of $Fe_3O_4@BH_4^-$ and $Ag@BH_4^-$ NPs with antioxidant activity by a homogenous and recyclable TAIm[BH_4] reductive ionic liquid: selective reduction of 4-nitrophenol to 4-aminophenol

Saade Abdalkareem Jasim[1] · Usama S. Altimari[2] · Halah T. Mohammed[3] · Mustafa K. Suhayb[4] · Abduladheem Turki Jalil[5] · Milad Kazemnejadi[6]

Received: 12 May 2022 / Accepted: 16 October 2022 / Published online: 31 October 2022

Abstract

An efficient and mild protocol was developed for the reduction of 4-nitrophenol to the 4-aminophenol in the presence of recyclable silver ($Ag@BH_4^-$ NPs) and magnetite nanoparticles ($Fe_3O_4@BH_4^-$ MNPs). The NPs were characterized by TEM, HRTEM, UV–Vis, TGA, VSM, XRD, EDX, XPS, and DLS analyses. The reduction was conducted in the absence of any external reducing agent like $NaBH_4$ underwent ultrasound irradiation at 60 °C for 2 h. Also, in the presence of TAIm[BH_4] ionic liquid, the reduction was performed under normal conditions (no need to ultrasound irradiation) and gave quantitative yield for 4-aminophenol at room temperature. TAIm[BH_4] ionic liquid (density = 1.42 g/cm^{-3}, viscosity = 1165 cP), as a new reducing agent was applied for the efficient preparation of $Ag@BH_4^-$ NPs and $Fe_3O_4@BH_4^-$ MNPs, with a mean diameter and zeta potential of 26 nm, 16 nm, and – 40 mV and – 55 mV, respectively. It was suggested that TAIm[BH_4] ionic liquid plays the role of a capping agent in addition to reducing capability in order to metal NPs preparation, which improves the dispersion stability of the NPs with a negatively charged zeta potential resulted in the decreased agglomeration of NPs. The NPs as well as TAIm[BH_4] ionic liquid showed high antioxidant activity evaluated by DPPH assay, which the total DPPH quenching was observed at 180 µg/mL. Also, TAIm[BH_4] IL showed a 70% inhibitory effect at a concentration of 200 µg/mL. The $Ag@BH_4^-$ and $Fe_3O_4@BH_4^-$ NPs follows first-order kinetics for the reduction of 4-NP with the reaction rate of (6.75×10^{-3} s^{-1}) and (5.6×10^{-3} s^{-1}), respectively. A reasonable mechanism was suggested based on the observation and literature review.

Graphical abstract

A new approach to synthesis of reductive Ag and Fe3O4 NPs with high antioxidant activity was introduced by TAIm[BH4] reductive ionic liquid for the efficient reduction of 4-NP to 4-AP.

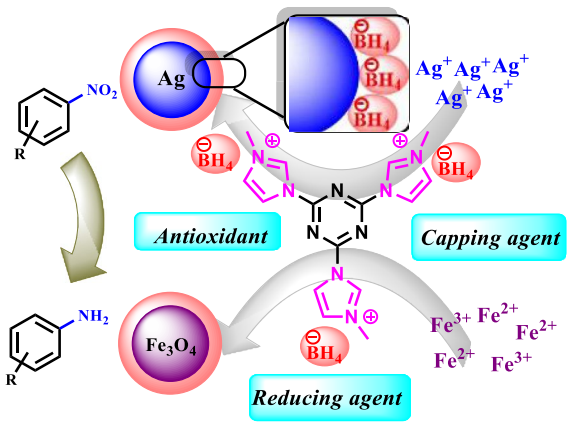

Extended author information available on the last page of the article

Keywords Nitroarene reduction · TAIm[BH_4] ionic liquid · Reducing agent · Ag@BH_4^- NPs · Fe_3O_4@BH_4^- MNPs · Antioxidant

1 Introduction

Nitro aromatic compounds such as 2-nitroanilline, picric acid, and nitrophenols are among the important pollutants that are toxic for human life, water, and environment due to non-biodegradable and stability, highly carcinogenic, and mutagenic nature. Nitro-aromatic compounds are widely used in industrial applications and so released into our natural environment [1, 2]. So, they need to post-treatment to cleaner products and/or eliminate from the nature. Various catalytic systems along with reducing agents have been developed for the reduction of 4-nitrophenol (4-NP) to 4-aminophenol (4-AP) selectively.

Metal nanoparticles, especially silver (Ag NPs) [3, 4] and magnetite (Fe_3O_4 NPs) nanoparticles, are one the most efficient and known catalytic systems for reducing 4-NP to 4-AP [3]. Metal nanoparticles are usually prepared by reducing the corresponding metal ions in the presence of a reducing agent, and their size and morphology depend on the concentration of the reducing agent as well as the reduction reaction conditions [5]. Various reducing agents were utilized for the preparation of metal NPs such as sodium borohydride ($NaBH_4$), sodium citrate, and extracts from different plant organs [5–7]. Aqueous extracts of different parts of plants, which are rich in phenolic compounds, are known as powerful reducing agents. However, the failure to obtain a single formulation, the failure to obtain a single percentage composition for a plant extract, and the failure to obtain the type of extract used by researchers in different parts of the world, severely limits the reproducibility of the method. Therefore, the use of synthetic reducing agents not only solves the mentioned limitations, but also, by designing a unique reducing agent, the morphology and catalytic properties of the resulting nanoparticle can be modified.

In addition to extracts of various plant organs, EtOH [6], apiin [8], starch [9], tin acetate [10], and gallic acid [11] have also been used as reducing agents to prepare Ag NPs.

Also, various reducing agents were also reported for the synthesis of Fe_3O_4 NPs such as α-d-glucose [12], citric acid [13], sodium citrate [14], ethylene glycol [15], and NaOH [16].

Despite these extensive advances in the preparation of Fe_3O_4 and Ag NPs, most of them, in addition to a reducing agent, require surfactants and capping agents in order to control the morphology and size distribution of the particles, which is not only affordable and environmentally friendly, but also changes the catalytic properties of the surface of the NPs. In addition, due to the low catalytic activity of Fe_3O_4 NPs [17], as well as Ag NPs [18], in order to use in catalytic systems requires surface modification with different compounds. Therefore, according to the wide and increasing applications of metal NPs in various fields of science [19–21], the development of an effective, reliable, and environmentally friendly method, in order to prepare metal nanoparticles in solution, is a basic need in industries and laboratory purposes. Moreover, these reductive systems cannot be manipulated and lead to a type of nanoparticles with fixed properties.

In last decade, ionic liquids (ILs) have been widely received the attentions to synthesize silver nanoparticles due to their NPs capping capability. ILs with their unique properties are able to create green chemical environments to perform chemical processes. The low vapor pressure of these compounds, unlike most organic solvents, makes them non-volatile and environmentally friendly compounds [22]. ILs generally consist of a bulk cation and an organic or inorganic anion that prevent the formation of a regular crystal lattice due to the poor concentration of the positive charge on the bulk cation. Therefore, although they are ionic in nature, they have a low melting point due to asymmetry in their molecular structure and are usually in liquid form at ambient conditions. These liquids are widely used in solar cells, synthesis of NPs, as electrolytes in electrochemistry [23], etc. [24]. Depending on the nature of their cations and anions, they can be used in special applications such as catalytic processes, metal extraction, surface modification, chemical sensors, and electrochemical systems. The high conductivity of ionic liquids compared to organic compounds makes them a good candidate for electrochemical reactions [23]. These compounds are able to form biphasic systems suitable for separation [25]. Therefore, the preparation of ionic liquid with a special catalytic property and or sensitive to ultrasonic and microwave irradiations eliminates the need for a solvent, and also for a catalytic system [26].

Metal NPs could be synthesized in ILs by chemical, physical, and electrochemical approaches [27]. ILs have remarkable properties as a sustainable media for stabilization of metal NPs via their electrostatic, tunable nature, and steric stabilization properties and in this way can improve their catalytic activity. ILs can act as stabilizers, solvents, reactants, and precursors for the growth of NPs [28]. So, the metal NPs could be prepared in ILs in the absence of any additional surfactant, stabilizer, and ligand [29]. The size and morphology is controlled by the surface composition/

organization of the ILs [30]. Previously, Qadir et al. synthesized naked Ag NPs with 5–8 nm in size in functionalized imidazolium-based ILs bearing cyano methoxy and thio groups by magnetron sputtering deposition [30]. They showed that the IL's counter ion effects on the preparation of Ag NPs. The same effects were observed for the preparation of Ag NPs from Ag ILs (silver(I) ionic liquids) with alkylethylenediamine ligands and $AgNO_3$-dissolving protic ionic liquids [31]. In another report, Ag NPs (< 10 nm) were prepared in 1-butyl-3-methylimidazolium-based ionic liquids bearing SbF_6^-, PF_6^-, and NTf_2^- as counter anions at room temperature [32]. Imidazolium-functionalized hyperbranched polymeric ionic liquids (HPILs) were also served as stabilizers in order to synthesis of Ag NPs [33].

ILs can also be used as a reducing agent to synthesis nanoparticles that was depended on the counter ion of ILs. Darwich et al. utilized dihydroxyl-functionalized ionic liquids (1-(2,3-dihydroxypropyl)-2,3-dimethylimidazolium bis(trifluoromethanesulfonimide)) as reducing agent for the synthesis of Ag NPs [34]. Also, citrate-based ILs were used as reducing and capping agents for the synthesis of colloidal Ag NPs (8 nm) [35].

Literature reports also demonstrated that ILs-assisted synthesized Ag NPs promotes the biological activity of NPs [36]. The synthesized Ag NPs in imidazolium iodide ILs improved antibacterial activity of the NPs against gram-positive and gram-negative bacteria [37]. Also, synthesized Ag NPs using hydroxyl-functionalized ILs (based on 1,3-disubstituted imidazolium cations and halogens anions) demonstrated high antimicrobial activity [38].

In our previous studies, 1,1′,1″-(1,3,5-Triazine-2,4,6-Triyl) tris(3-methyl-1*H*-Imidazol-3-ium) iodide ionic liquid (TAIm[I] IL) was prepared via a simple procedure based on a triazine skeleton [39–41]. The prepared structure makes it possible to prepare ionic liquids containing different counter ions. For example, in the presence of Ag_2O, it was transferred to a basic ionic liquid (TAIm[OH] IL) and effectively used in the transesterification as well as aldol condensation [40]. Also, as a strong ligand in the presence of Pd ions, various types of coupling reactions were catalyzed in the presence of this ionic liquid [24–41]. This paper introduces a novel reductive ionic liquid, briefly named as TAIm[BH_4] IL (1,1′,1″-(1,3,5-Triazine-2,4,6-Triyl) tris(3-methyl-1*H*-Imidazol-3-ium) borohydride ionic liquid), with high antioxidant activity for the preparation of Ag and magnetite NPs by its reducing and capping property. The resulting Ag and magnetite NPs was found as highly efficient catalyst toward the reduction of 4-NP to 4-AP under mild conditions in TAIm[BH_4] ionic liquid as a solvent, so their name was changed to $Ag@BH_4^-$ and $Fe_3O_4@BH_4^-$ NPs. This reduction could be taken place in the absence of TAIm[BH_4] IL under ultrasound irradiation. TAIm[BH_4] ionic liquid was also showed as a suitable solvent for this transformation. Kinetics and mechanism of the reduction was studied for both NPs. TAIm[BH_4] IL as a reducing agent provides the possibility of preparing nanoparticles without the need of capping agent and surfactant. Also, by manipulating this ionic liquid, it is possible to prepare nanoparticles with desired properties.

2 Experimental

2.1 Materials and instrumentation

Cyanurchlorid (TCT, Sigma-Aldrich, 99%), NaI (Sigma-Aldrich, ≥ 99.0%), 1-Methylimidazol, Sigma-Aldrich, ReagentPlus® ≥ 99%, $NaBH_4$ white powder (Sigma-Aldrich, ≥ 98.0%), $AgNO_3$ (FUNCMATER, 99.8%), $FeCl_3{\cdot}6H_2O$ (Sigma-Aldrich, reagent grade, ≥ 98%, chunks), $FeCl_2{\cdot}4H_2O$ (Sigma-Aldrich, puriss. p.a., ≥ 99.0% RT), 4-nitrophenol (Tokyo Chemical Industry Co., Ltd., > 99.0%).

P30H Ultrasonic Bath with heater, drain, 0.7 Gal, Int. dim. 9.4" × 5.4" × 3.9" (LxWxH), 115 V, Thomas Scientific (USA) was used for applying the reactions under ultrasonic waves. Zeta potential and size distribution of $Ag@BH_4$ and $Fe_3O_4@BH_4$ NPs were estimated using the dynamic light scattering (DLS) method on a Malvern Zetasizer nano-series HT Nano-25 apparatus, ver. 6.32, Malvern Instruments Ltd., Malvern, Worcestershire, UK. Gas chromatography analyses were performed on an YL 6100 gas chromatograph system (GC) with a CBP5 column (Shimadzu 30 m × 0.32 mm × 0.25 mm). The viscosity of the ionic liquids was measured using a Thermo Scientific™ HAAKE™ Viscotester™ apparatus at room temperature. Elemental analysis of the samples was performed on an energy-dispersive X-ray (EDX) Oxford X-Max, Oxford, UK instrument. Morphology of the NPs was studied by the field emission scanning electron microscopy (FE-SEM) technique using a Tescan MIRA3 145 apparatus. XPS analyses were performed using a XR3E2 (VG Microtech) twin anode X-ray source (with radiation of Al-$K\alpha$ = 1486.6 eV). Thermogravimetric analyses (TGA) of the samples were performed on a NETZSCH STA 409 PC/PG under N_2 atmosphere with a heating rate of 10 °C/min. Crystal structure of the NPs was studied by X-ray diffraction (XRD) patterns of the NPs on a Rigaku Smart-Lab X-ray diffractometer with Cu Kα (λ = 1.5418 nm) radiation. HRTEM images were taken on a FEI Tecnai G2 F20 Super Twin TEM with a field emission gun at 200 kV. Transmission electron microscopy (TEM) images of the NPs were taken using a Philips EM208 microscope and were operated at 100 kV. Vibrating sample magnetometer (VSM) measurements of $Fe_3O_4@BH_4$ NPs were taken by using a BHV-55 vibrating sample magnetometer. X-ray photoelectron spectroscopy (XPS) measurements were taken on a XR3E2 (VG Microtech) twin anode X-ray source

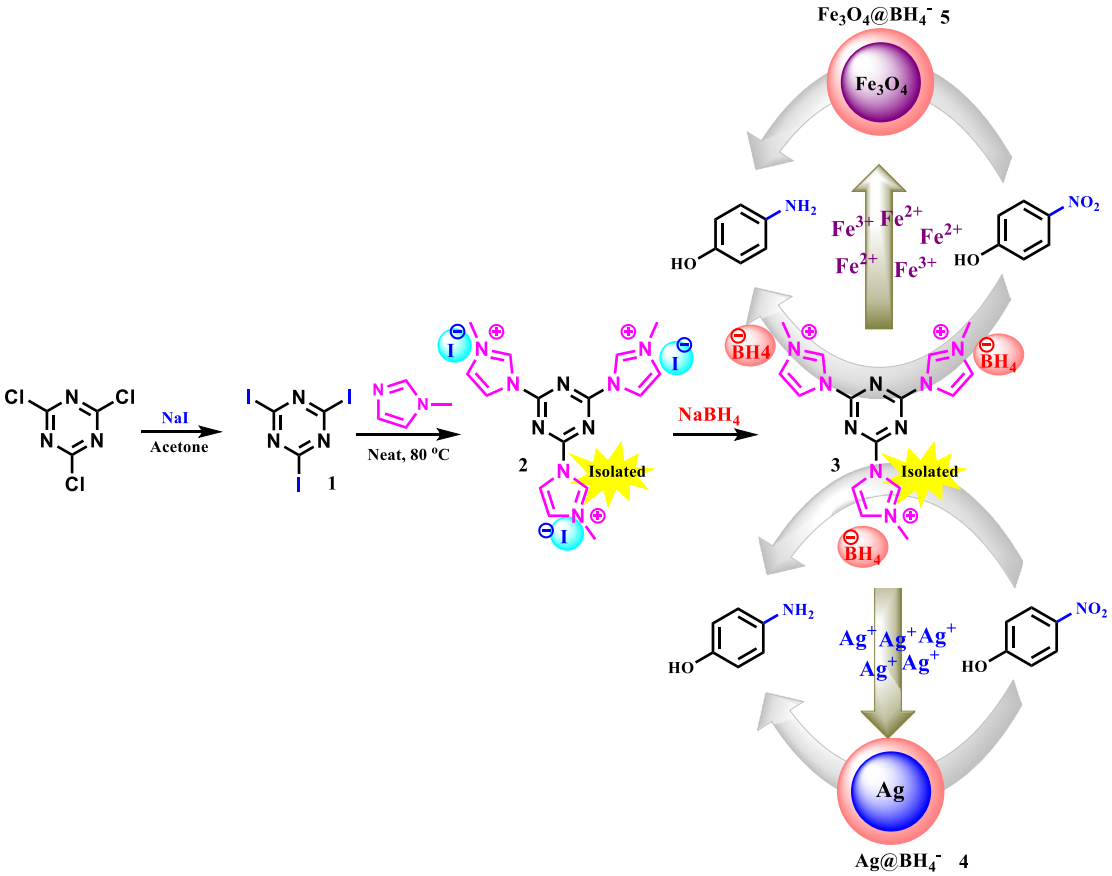

Scheme 1 Preparation of TAIm[BH_4] IL (**3**) as a reducing and capping agent for the preparation of Ag@BH_4^- (**4**) and Fe_3O_4@BH_4^- NPs (**5**)

with AlKα = 1486.6 eV. UV–Vis analyses were performed on a UV Spectrolab BEL photonics instrument.

2.2 Synthesis of 1,1′,1″-(1,3,5-Triazine-2,4,6-Triyl) tris(3-methyl-1*H*-Imidazol-3-ium) iodide (TAIm[I]) (2) and TAIm[BH_4] (3)

TAIm[I] IL was prepared in two steps according to our previously reported protocols [39–41]. TAIm[BH_4] IL was prepared and isolated simply by dissolution of 2.5 mL TAIm[I] (6.5 mmol) in 2.0 mL of distilled water at ambient temperature. Then, $NaBH_4$ salt (7.0 mmol) was added to the solution, and the mixture was stirred for 4 h. The mixture was filtered, and the resulting TAIm[BH_4] IL was extracted to *n*-BuOH from the residue three times (each 5.0 mL). Finally, the solvent was removed under reduced pressure and the product was isolated at 4 °C (Scheme 1).

2.3 TAIm[BH_4]-mediated synthesis of Fe_3O_4@BH_4^- magnetic NPs

Fe_3O_4@BH_4^- magnetic NPs was prepared using a wet chemical reduction approach via the co-precipitation of ferric ions [42–45]. An aqueous solution (500 mL) of $FeCl_3.6H_2O$ (1.3 g, 4.8 mmol) and $FeCl_2.4H_2O$ (0.9 g, 4.5 mmol) was prepared, and the solution temperature was adjusted to 70 °C. Then, TAIm[BH_4] IL 2.5 M (10.0 mL) was added dropwise to the ferric solution during stirring at 70 °C. The addition was done during 30 min, and the solution became darker gradually, which after complete addition of TAIm[BH_4] IL, the solution turned to black. Then, the mixture was stirred for further 4.0 h. Finally, the resulting Fe_3O_4@BH_4^- MNPs were separated from the mixture by applying an external magnetic field (N42-40–20 super strong neodymium magnet, Magnet Gostar Arya, IRAN), washed with deionized water and ethanol, then dried and stored at room temperature (Scheme 1).

2.4 TAIm[BH_4]-mediated synthesis of Ag@BH_4^- NPs

Ag@BH_4^- NPs was prepared by a same procedure described for Fe_3O_4@BH_4^- MNPs by the reduction of silver ions ($AgNO_3$ 1.0 g in 500 mL distilled water). The resulting NPs was separated and purified by centrifugation and several washing with deionized water and ethanol, then dried and stored at room temperature (Scheme 1).

2.5 Ultrasound-mediated $NaBH_4$-free reduction of 4-NP to the 4-AP catalyzed by $Ag@BH_4^-$ and $Fe_3O_4@BH_4^-$ NPs in water

In a reaction tube, 1.0 mmol of 4-NP and 5.0 mg of $Ag@BH_4^-$ (10.0 mg for $Fe_3O_4@BH_4^-$) were added to H_2O (2.0 mL). The reaction was performed in the absence of $NaBH_4$ at 60 °C in a water bath under ultrasonic conditions. The reduction progress was monitored by TLC technique, and also UV–Vis analysis. After the complete reduction of 4-NP to 4-AP, the ultrasound irradiation was stop, and the mixture was cooled to room temperature. The catalyst was separated by centrifugation (or using an external magnet in the case of $Fe_3O_4@BH_4^-$ NPs), washed with deionized water (3 × 5 mL, centrifugation) and ethanol (3 × 5 mL, centrifugation), then dried and stored for the next run.

2.6 Mild reduction of 4-NP catalyzed by $Ag@BH_4^-$ and $Fe_3O_4@BH_4^-$ NPs in the presence of TAIm[BH_4] reductive ionic liquid as a solvent

By changing solvent of the reduction reaction from water to TAIm[BH_4] IL (2.0 mL), the reduction of 4-NP catalyzed by $Ag@BH_4^-$ and $Fe_3O_4@BH_4^-$ NPs was performed at room temperature without any external driving force like ultrasound irradiation. The reduction progress was monitored by TLC technique. The NPs was recovered from the mixture by centrifugation, washed with deionized water and EOH and reused for the next cycle after drying. TAIm[BH_4] IL could also be recycled from the reaction mixture by addition of 5.0 mL of distilled water and 5.0 mL of EtOAc to the reaction mixture after NPs recovering. The water was removed from the aqueous layer containing TAIm[BH_4] IL, and the recycled TAIm[BH_4] IL was stored at 4 °C for the next use (Scheme 1).

2.7 Catalyst-free reduction of 4-NP to 4-AP in the presence of TAIm[BH_4] reductive ionic liquid as a solvent

Also, in another protocol, the reduction of 4-NP was performed in the absence of catalyst and in the presence of TAIm[BH_4] reductive ionic liquid as a solvent (as a control experiment). The catalyst-free reduction of 4-NP to 4-AP was performed at 120 °C underwent ultrasound irradiation for 2.0 h (Scheme 1).

2.8 Antioxidant (antiradical) activity

Antioxidant activity of the synthesized NPs and ILs was measured using 2,2-diphenyl-1-picrylhydrazyl (DPPH) radical scavenging assays according to a previously reported standard procedure [46]. In first, various concentrations of aqueous NPs and ILs were prepared (10, 30, 50, 70, 100, 120, 140, 160, 180, 200 µg/mL), and for each experiment, 75 µL of each sample was added to 3.9 mL of 0.00463 g/L DPPH solution. The resulting solution was stirred for 45 min in a dark place, then, the absorbance of the solutions was recorded at 517 nm. The %inhibition of the samples was calculated using following Eq. (1) [46, 47]:

$$\%\text{Inhibition} = \frac{A_{\text{blank}} - A_{\text{sample}}}{A_{\text{blank}}} \times 100 \quad (1)$$

Standard ascorbic acid was used as a positive control. The efficiency of antioxidant activity was expressed as the IC_{50} value known as half maximal effective concentration to scavenge 50% of free radicals.

3 Results and discussion

First, the formation of TAIm[BH_4] IL from TAIm[I] IL was studied by EDX analysis (Fig. S1). TAIm[BH_4] IL, after reaction with $NaBH_4$ in aqueous medium, was extracted by *n*-butanol and studied by EDX analysis. The results significantly confirmed the presence of I element in the resulting IL (**2**) at 3.9, 4.1, 4.5, 4.9 keV binding energies, respectively, related to ($L\alpha_1$, $L\alpha_2$), $L\beta_1$, $L\beta_2$, $L\gamma_1$, totally equal to 54.59%wt, in agreement with the theoretical calculation. The presence of B element-related peak at 0.2 keV and also complete elimination of I element-related peaks in the EDX spectrum of TAIm[BH_4] (Fig. S1b), indicated the formation of TAIm[BH_4] IL by replacing iodide by BH_4^- (Scheme 1).

Table 1 shows the physical properties of TAIm[BH_4] and TAIm[I] IL including appearance, viscosity, and density. According to the results, TAIm[BH_4] and TAIm[I] ILs have density of 1.68 and 1.42 g.cm^{-3}, respectively. Also,

Table 1 Physical properties of TAIm[BH_4] and TAIm[I] ILs

Ionic liquid		Physical properties		
	Mw (g.mol^{-1})	Color/appearance	Density (g.cm^{-3})	Viscosity (cP)
TAIm[I]	705.0	Dark yellow oil	1.84[a]	1182
TAIm[BH_4]	368.9	Colorless oil	1.42[b]	1165

[a]Based on apparatus. 1.87 g.cm^{-3} from the acid titration assay

[b]Based on apparatus. 1.72 g.cm^{-3} from the acid titration assay

the viscosity of the ILs was calculated as 1194 and 1165 cp, respectively.

3.1 Characterization of NPs

Figure 1 shows the EDX and XPS (overall survey) of Ag@BH_4^- NPs and Fe_3O_4@BH_4^- MNPs. The presence of the expected elements in both NPs clearly confirmed their preparation as Ag@BH_4^- and Fe_3O_4@BH_4^- structures. B element could be found in the EDX (Fig. 1a, b) as well as XPS spectra (Fig. 1c, d), which confirm the presence of B element in the structure of the NPs. In addition, the presence of C, N, and O elements in both EDX and XPS spectra confirms the presence of TAIm[BH_4] IL species on the surface of the NPs. Five characteristic peaks at 9.45, 97.93, 717.22, 729.18, and 788.30 eV were assigned to Fe3d, Fe3s, $Fe2p_{3/2}$, $Fe2p_{1/2}$, and FeLMM (Auger peak), respectively, in the XPS spectrum of Fe_3O_4@BH_4^- [48]. The ratio of C/N, C/O, and N/O elements was quite similar to the ratio obtained for TAIm[BH_4] IL elemental analysis (Fig. 1 a, b), and it can be concluded that the TAIm[BH_4] IL molecules were located/immobilized on the surface of the NPs as a capping agent without any change in the structure of the NPs. The results indicated the capping agent property of TAIm[BH_4] IL as well as the reducing activity toward Ag and Fe metal ions. As shown in Fig. 1, the EDX and XPS analyses were in good agreement with each other, reflecting the high purity of the NPs and the high accuracy of the results. The prominent point was the high purity of the prepared nanoparticles, so that no additional element due to impurities was detected in the EDX and XPS spectra. Figures S2, S3 show the EDX-elemental mapping of Ag@BH_4^- NPs and Fe_3O_4@BH_4^- NPs. The EDX-elemental mapping of Ag@BH_4^- NPs and Fe_3O_4@BH_4^- NPs represents that the distribution of the elements in the structure of the NPs is monotonous (Figs. S2, S3) [49]. As shown in Figs. S2, S3, B element well distributed in the NPs structures that provides a uniform interaction of 4-NP with the NPs surface.

TEM analysis of the NPs showed that both Ag@BH_4^- and Fe_3O_4@BH_4^- NPs have a homogeneous morphology with

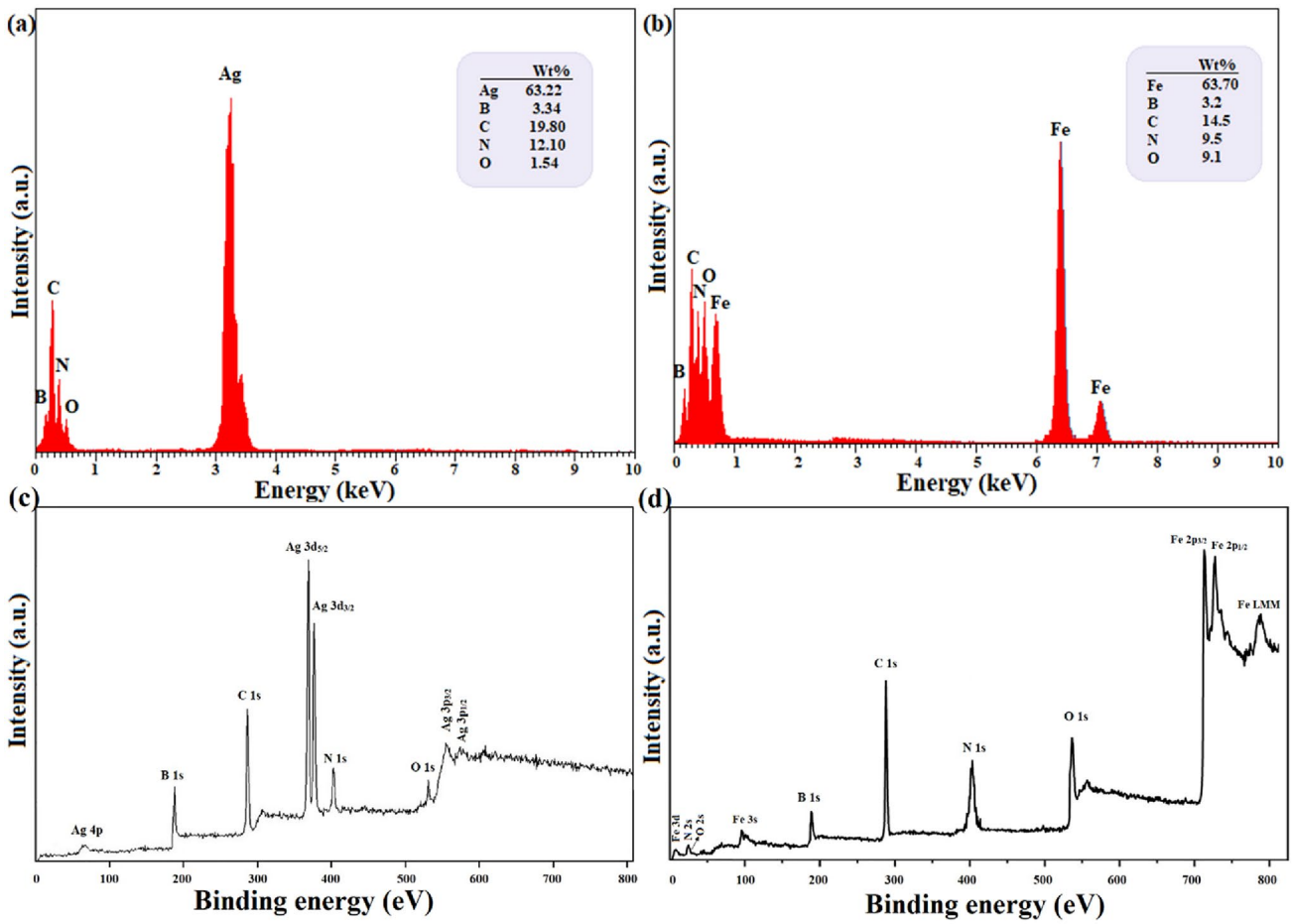

Fig. 1 EDX and XPS (overall survey) spectra of **a**, **c** Ag@BH_4^- NPs and **b–d** Fe_3O_4@BH_4^- magnetic NPs, respectively. The inset tables represent the mean of 5 points of the elemental analysis of the NPs obtained by EDX instrument

almost spherical shape and a mean diameter size equal to 26 nm and 16 nm, respectively (Fig. 2 a, b). The homogeneous morphology and non-agglomeration of the NPs can be attributed to the capping effect of TAIm[BH_4] IL, which by creating a double electrical layer around the nanoparticles [28, 29, 35], causes the crystals to grow and also not agglomerate to each other. The TAIm[BH_4] IL promotes the growth of small Ag microcrystals and was responsible for the larger size observed for the NPs. The structure of the NPs also confirmed by HRTEM images along with SAEM pattern (as inset images) in agreement with the literature [28, 29, 35] (Fig. 2 c, d).

DLS particle size distribution study showed that both $Ag@BH_4^-$ and $Fe_3O_4@BH_4^-$ NPs have a narrow size distribution and the major particles have a hydrodynamic diameters of 30 and 22 nm for $Ag@BH_4^-$ and $Fe_3O_4@BH_4^-$ NPs, respectively (Fig. 3). The difference in diameter size observed for the NPs can be attributed to the coating/immobilizing of the ionic liquid layer on the surface of the NPs as a capping agent. Also, the presence of the IL on the surface of NPs has caused a significant negative zeta potential for them. As shown in Fig. 3, $Ag@BH_4^-$ and $Fe_3O_4@BH_4^-$ NPs have zeta potential of – 40 and – 55 mV, respectively. These high negative values for the zeta potential of NPs ensure the stability and ease of dispersion of the NPs in the medium.

Figure 4A shows the crystal structure of $Ag@BH_4^-$ and $Fe_3O_4@BH_4^-$ NPs. X-ray diffraction pattern of $Ag@BH_4$ NPs represents five characteristic peaks at $2\theta = 28.5°$, 38.3°, 44.4°, 64.5°, and 77.4°, respectively, corresponding to the indices/lines of (110), (111), (121), (200), and (311), which was completely in agreement with the X-ray diffraction pattern of pure Ag NPs (JCPDS file No. 89–3722) with a Fm-3 m space group [50] as well as the published articles (Fig. 4a) [17, 18]. Also, the crystal structure of Fe_3O_4 NPs was confirmed by six characteristic peaks at $2\theta = 30.3°$,

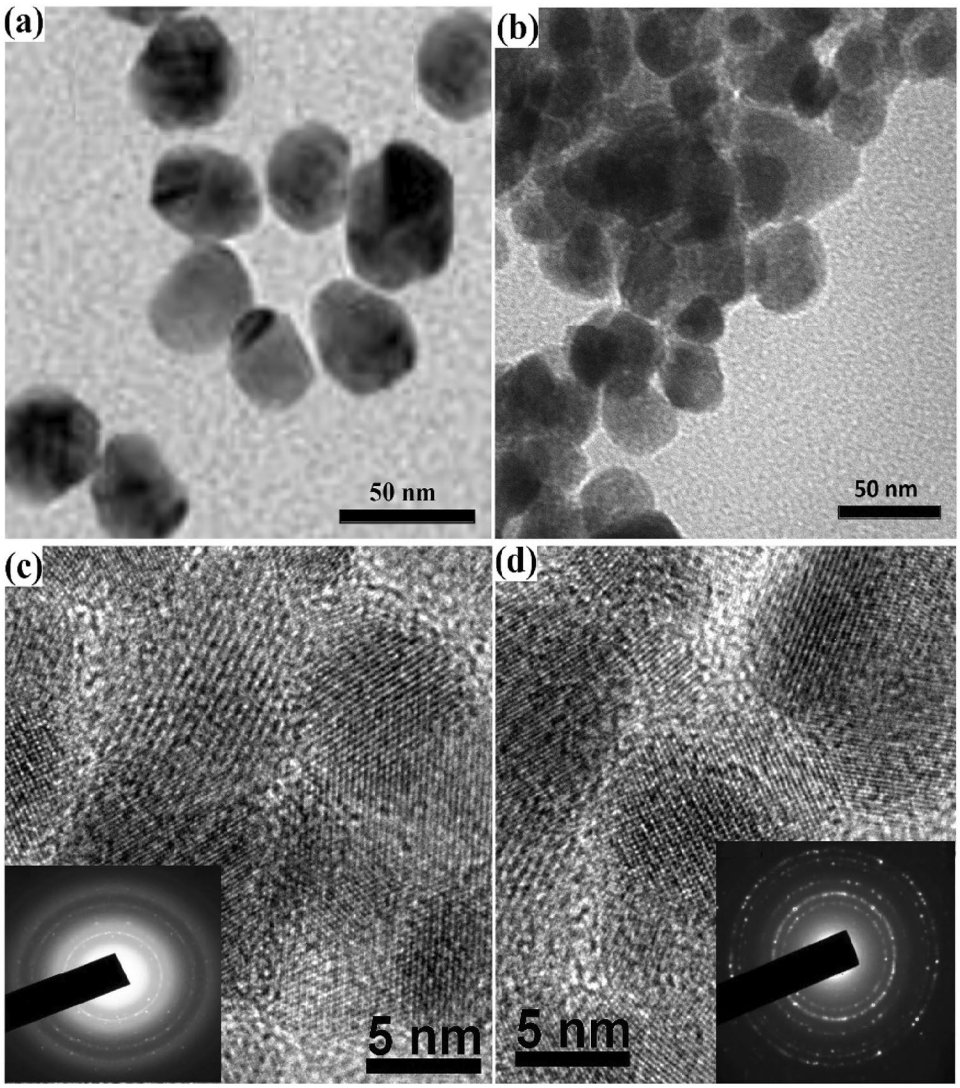

Fig. 2 **a**–**b** TEM and **c**–**d** HRTEM images of $Ag@BH_4^-$ and $Fe_3O_4@BH_4^-$ NPs, respectively

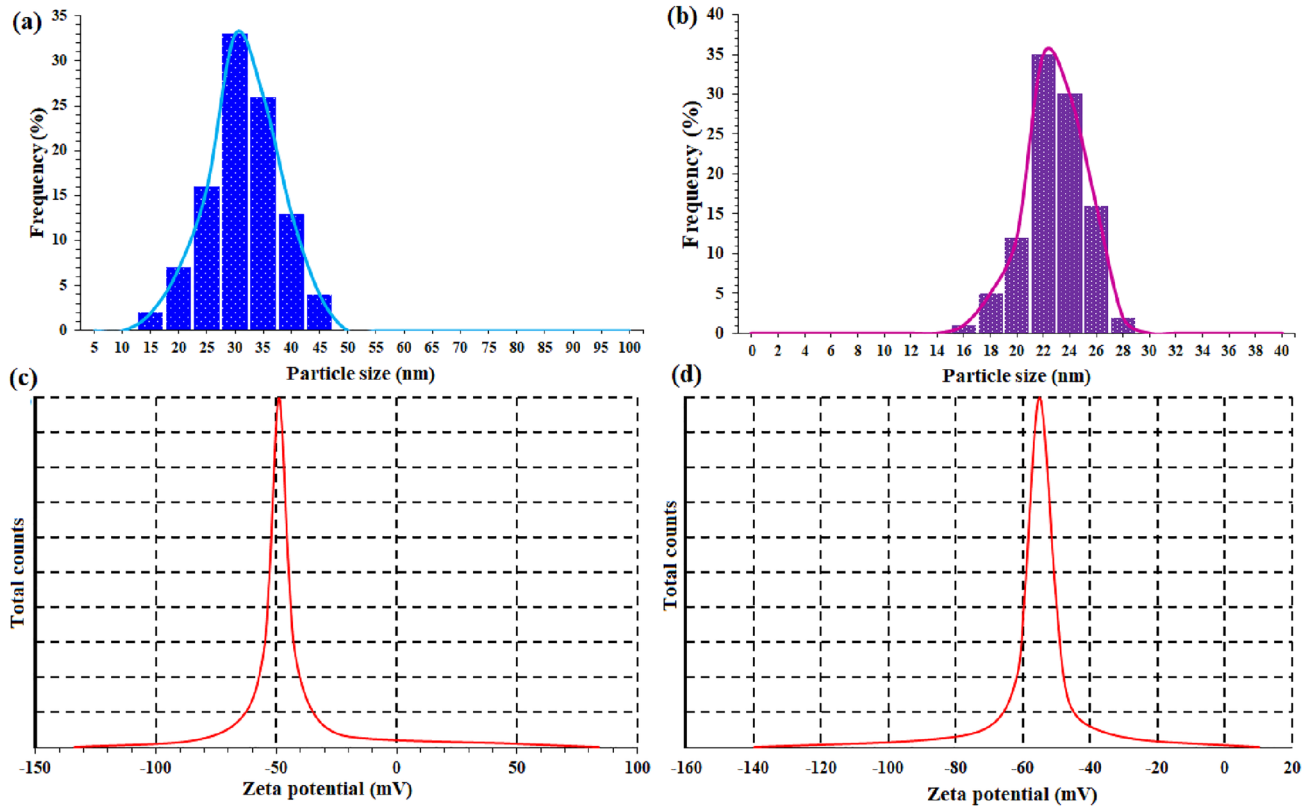

Fig. 3 **a**–**b** Hydrodynamic size distributions and (**c**),(**d**) zeta potential measurement of $Ag@BH_4^-$ and $Fe_3O_4@BH_4^-$ NPs, respectively

35.6°, 43.1°, 53.4°, 57.2°, and 62.5° related to the (220), (311), (400), (422), (511), and (440) planes, respectively, demonstrating the Fe_3O_4 crystal structure in agreement with the X-ray diffraction pattern of pure Fe_3O_4 NPs (PDF#88–0866, reference JCPDS card no. 19–629) with a Fd3m space group [51] as well as published articles [25, 26] (Fig. 4A–b).

As shown in the X-ray diffraction patterns of the NPs, compared to the X-ray diffraction patterns reported from uncoated Ag [52] and Fe_3O_4 [53] NPs, the $Ag@BH_4^-$ and $Fe_3O_4@BH_4^-$ X-ray diffraction patterns deviate somewhat from the ideal crystalline state, which can be directly attributed to the immobilized TAIm[BH_4] IL layer on the NPs surfaces as a capping agent.

The nanoparticles microcrystalline diameter were also measured by Scherer's Eq. (2) [54, 55]:

$$D = \frac{k\gamma}{\beta \mathrm{Cos}\theta} \tag{2}$$

where D is the average diameter (in Å), k is a constant equal to 0.9 (for Cu Kα), β is the broadening of the diffraction peak measured at half of its maximum intensity (in radians), γ is the wavelength of the X-rays, and θ is the Bragg diffraction angle [43, 56]. According to Eq. 1, the size of microcrystals for $Ag@BH_4^-$ and $Fe_3O_4@BH_4^-$ was calculated as 19 and 10 nm, respectively. The observed size difference for the nanoparticles compared to the higher sizes in DLS and TEM was another confirmation of the functionalization of the nanoparticle surface with the TAIm[BH_4] IL. Also, microstrain (ε), dislocation density (ρ_D), and lattice parameter (a) for the NPs were calculated using the following equations [57–61]:

$$\varepsilon = \frac{\beta_{2\theta}}{4\tan\theta} \tag{3}$$

$$\rho_D = \frac{1}{D^2} \tag{4}$$

$$a = d\sqrt{h^2 + K^2 + l^2} \tag{5}$$

where D is the crystalline size calculated using Scherer's equation. Also, h, k, and l represent the Miller indices and d is the inter planer spacing. Table 2 shows the microstrain ε, dislocation density (m^{-2}), and lattice parameter a (nm) for both $Ag@BH_4^-$ and $Fe_3O_4@BH_4^-$ NPs. Microstrain for $Ag@BH_4^-$ and $Fe_3O_4@BH_4^-$ NPs was calculated as 0.00414 and 0.00841, respectively. Also, dislocation density for them was found to be 2.77×10^{15} m^{-2} and 10^{16} m^{-2}, respectively.

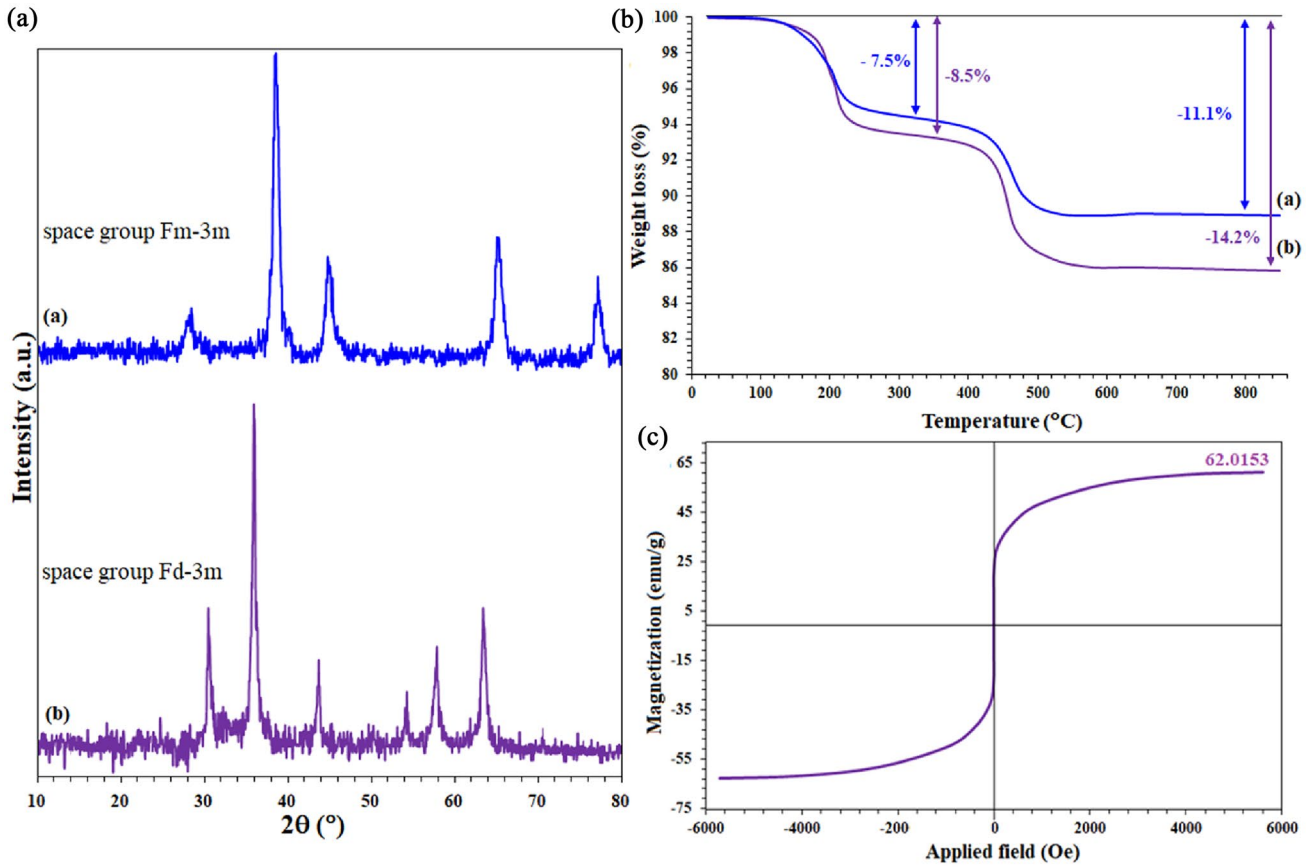

Fig. 4 A XRD pattern and B TGA analyses of **a** $Ag@BH_4^-$ and **b** $Fe_3O_4@BH_4^-$ NPs. **C** VSM analysis of $Fe_3O_4@BH_4^-$ NPs

Table 2 Calculated values of microstrain (ε), dislocation density (ρ_D), and lattice parameter (a) of $Ag@BH_4^-$ and $Fe_3O_4@BH_4^-$ NPs

NPs	2θ (°)	Parameters		
		microstrain ε	Dislocation density ρ_D (m^{-2})	Lattice parameter a (nm)
$Ag@BH_4^-$	38.3	0.00414	2.77×10^{15}	0.406
$Fe_3O_4@BH_4^-$	35.6	0.00841	10^{16}	0.286

Using Eq. (5), the lattice parameter (a) for the NPs was determined as 0.406 and 0.286, respectively.

Almost the same thermal behavior was observed for $Ag@BH_4^-$ and $Fe_3O_4@BH_4^-$ NPs. As shown in Fig. 4B, two weight losses in the temperature range of 220 °C and 420 °C were observed in the TGA analysis of the NPs. Due to the water solubility of TAIm[BH_4] IL and also its capping capability in the stability of the NPs, the observed weight losses equal to 7.5% and 11.1% in the temperature range of 220 °C and 420 °C could be related to the ionic liquid scape from the surface and the lattice structure of the $Ag@BH_4^-$ NPs, respectively. Exactly the same temperature behavior was observed for $Fe_3O_4@BH_4^-$ NPs in accordance with the weight losses of 8.5% and 14.2% in the same temperature ranges. The thermal behavior of the NPs was completely correlated with other results of characterization: The greater weight loss in $Fe_3O_4@BH_4^-$ NPs indicates more ionic liquid coating (as a reducing and capping agent) on the surface of the $Fe_3O_4@BH_4^-$ NPs, resulting in smaller size and consequently more aspect ratio than $Ag@BH_4^-$.

VSM analysis of $Fe_3O_4@BH_4^-$ NPs shows the superparamagnetic behavior with a saturation magnetization equal to 62 emu/g and zero coercivity (Fig. 4C), in agreement with the magnetic behavior of Fe_3O_4 NPs prepared by other methods [42]. $Fe_3O_4@BH_4^-$ NPs have good magnetic properties, so that by applying an external magnetic field (by a N42-40–20 super strong neodymium magnet) they can be separated from the reaction mixture for 20–30 s.

Considering the results of EDX and XPS analyses and proving the presence of BH_4^- groups as well as TAIm[BH_4] IL on the NPs surfaces, it was shown that TAIm[BH_4] IL acts not only as a reducing agent for Ag and Fe ions, but also plays the role of a capping agent and prevents the agglomeration of nanoparticles. This dual function of TAIm[BH_4] IL is shown in Scheme 2.

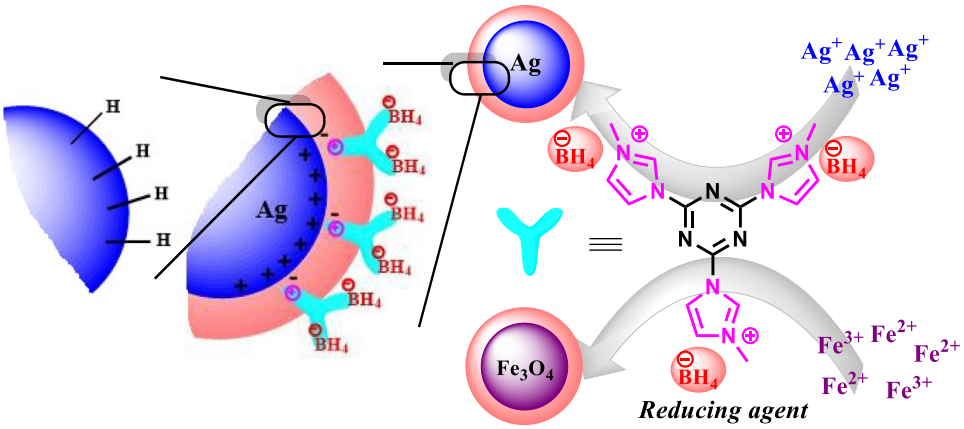

Scheme 2 Efficient preparation of $Ag@BH_4^-$ and $Fe_3O_4@BH_4^-$ NPs using TAIm[BH_4] IL as reducing and capping agent

3.2 Screening of reaction parameters

The effect of three parameters of temperature, catalyst amount, and solvent type on the reduction of 4-NP catalyzed by $Ag@BH_4^-$ and $Fe_3O_4@BH_4^-$ NPs was studied. TAIm[BH_4] was used as solvent and hydrogen source (reductant) in all reactions. Figure S4 shows the effect of these three parameters. Temperature had no significant effect on reduction efficiency, and the best efficiency was obtained at room temperature. The highest efficiency was observed at 50 mg and 100 mg of $Ag@BH_4^-$ and $Fe_3O_4@BH_4^-$ NPs, respectively, and at higher values the efficiency decreased slightly (Figure S4a). This decrease in efficiency can be attributed to the agglomeration of NPs in higher amounts due to their high surface-to-volume ratio [62]. The study of the effect of different solvents is shown in Figure S4b. The low to medium efficiency for solvents other than TAIm[BH_4] IL showed that the NPs alone can reduce 4-NP in the absence of any external reducing agent. This effect can be directly attributed to the property of the ionic liquid as a capping agent during the preparation of the NPs, which caused the NPs to be coated with a layer of TAIm[BH_4] IL as well as the protonation of their surface. The results were completely consistent with the results of the NPs characterization, which confirmed the presence of H and the ionic liquid on the surface of the NPs. However, the conversion percentage for 4-NP in these solvents was very low, and the efficiency was observed only in the presence of ultrasonic waves. Ultrasonic waves seem to provide the energy needed to absorption of 4-NP on the surface of NPs as well as crossing the electrical double layer (Scheme 2). However, in the presence of TAIm[BH_4] IL and in the absence of ultrasonic waves, 4-NP reduction was catalyzed completely by the NPs. TAIm[BH_4] IL not only acts as a reducing agent and reaction solvent, but also stabilizes the 4-nitrophenlate anion, causing its rapid penetration and easy adsorption on the surface of the NPs.

Table 3 shows the results of the optimization experiments of different protocols for 4-NP reduction. In the absence of any reducing agent and under ultrasonic conditions, $Ag@BH_4^-$ and $Fe_3O_4@BH_4^-$ NPs gave 92% and 75% efficiency for 2 h, respectively. The difference in catalytic activity of $Ag@BH_4^-$ and $Fe_3O_4@BH_4^-$ NPs can be directly attributed to the nature of the NPs and their intrinsic properties

Table 3 Catalytic performance of Ag@BH4 – and Fe3O4@BH4 – NPs at various conditions

Entry	Catalyst	Solvent	Temp. (°C)	Conditions	Time (min)	Conversion (%)[b]
1	$Ag@BH_4^-$	H_2O	60	Ult	120	92[c]
2		H_2O	60	-	120	12
3	$Fe_3O_4@BH_4^-$	H_2O	60	Ult	120	75[d]
4		H_2O	60	–	120	7
5	$Ag@BH_4^-$	TAIm[BH_4]	R.T	–	60	100
6	$Fe_3O_4@BH_4^-$	TAIm[BH_4]	R.T	–	80	100
7	–	H_2O	60	Ult. or not[e]	120	0
8	–	TAIm[BH_4]	120	Ult	120	20

[a]Reaction conditions: 4-Nitrohenol (1.0 mmol). Catalyst amount: $Ag@BH_4^-$ (5.0 mg), $Fe_3O_4@BH_4^-$ (10.0 mg). Solvent: 2.0 mL. [b]GC yield. [c]44% for 60 min. [d]30% for 80 min. [e]There was not any difference under Ult. and normal conditions

(Table 3, entries 1–6). However, $Fe_3O_4@BH_4^-$ NPs in the presence of TAIm[BH_4] IL gave complete conversion for 4-NP for 80 min. As shown in Table 3, 4-NP converts completely (100% conversion) to 4-AP in the presence of $Ag@BH_4^-$ and $Fe_3O_4@BH_4^-$ NPs in TAIm[BH_4] for 60 and 80 min, respectively. The results showed the dependence of the NPs on the reduction of 4-NP under ultrasonic conditions in the absence of TAIm[BH_4] IL (Table 3, entry 1–4). In the absence of ultrasonic waves, the efficiency for $Ag@BH_4^-$ and $Fe_3O_4@BH_4^-$ NPs decreased to 12 and 7%, respectively. As will be explained in the mechanical studies, the presence of an electrical double layer of the IL on the surface of the NPs, as a result of their formation in the presence of TAIm[BH_4] IL, causes the 4-NP substrate to not penetrate well on the surface of the NPs and also do not have enough energy to properly interact with the surface. The reaction in the absence of NPs in aqueous solvent had no efficiency even under ultrasonic conditions (Table 3, entry 7), which indicates the catalytic activity of $Ag@BH_4^-$ and $Fe_3O_4@BH_4^-$ NPs in the reduction of 4-NP. However, a low efficiency was observed in the presence of TAIm[BH_4] IL under ultrasonic conditions (Table 3, entry 7), which indicates the reductive ability of TAIm[BH_4] IL even in the absence of the NPs.

The reactions were carried out at the normal pH of the reaction (equal to pH 7.3) as optimal conditions. In order to investigate the effect of pH in the reduction of 4-NP, the reaction was studied at different pHs of 3, 5, 7, 9, 11, and 13 adjusted by 0.1 N NaOH and 0.1 N HCl. Considering that, in the conditions used in the presence of TAIm[BH_4] IL, the reaction took place in the absence of water, the study of the effect of pH in the aqueous environment was studied under ultrasonic conditions in water. Table 4 shows the results of this study in terms of conversion obtained by GC. In agreement with the previous report [63], neutral pH was the best condition for the reduction of 4-NP, and the efficiency decreases at higher and lower pHs. In acidic pHs, due to the shift of the zeta potential for nanoparticles toward positive values and their subsequent agglomeration [64], it suffers a greater drop in productivity than at basic pHs. Also, acidic pHs prevent the formation of phenolate species as the active intermediates in the reduction of 4-NP. On the other hand, as the environment becomes more alkaline at pHs 9–13, the efficiency also decreases. This reduction was probably due to the interference of proton transfer from the surface of nanoparticles to 4-NP by OH groups.

Table 4 Effect of pH on the catalytic reduction of 4-NP to 4-AP by $Ag@BH_4^-$ and $Fe_3O_4@BH_4^-$ under ultrasound irradiation in water

Entry	Catalyst	pH	Conversion (%)[a]
1	$Ag@BH_4^-$ [b]	3	35
2		5	62
3		7	92
4		9	91
5		11	82
6		13	80
7	$Fe_3O_4@BH_4^-$ [c]	3	25
8		5	44
9		7	75
10		9	70
11		11	70
12		13	62

[a] GC yield. [b] Reaction conditions: 4-Nitrohenol (1.0 mmol), $Ag@BH_4^-$ (5.0 mg), H_2O (2.0 mL), 60 °C, Ultrasonic irradiation, 120 min. [c]Reaction conditions: 4-Nitrohenol (1.0 mmol), $Fe_3O_4@BH_4^-$ (10.0 mg), TAIm[BH_4] (2.0 mL), 60 °C, Ultrasonic irradiation, 120 min

In order to study the effect of TAIm[BH_4] IL in more depth, the reduction of 4-NP at different times intervals was studied by UV–Vis analysis. The zeta potential of NPs was also measured at similar times. Figure 5A shows the results of these analyzes for $Ag@BH_4^-$ and $Fe_3O_4@BH_4^-$ NPs in the presence of TAIm[BH_4] IL. As shown in Fig. 5 the absorption of 4-NP and 4-AP was appeared at 420 nm and 318 nm, respectively, which, compared to the previous reports based on NaH_4 reduction [65], the corresponding peaks had red shift (bathochromic) of about 20 nm. The results show the formation of stable TAIm[4-introphenolate] intermediate, which was more stable than O_2N-Ph-O^-Na^+ species. As shown in the figures, from the first minute, 4-NP reduction was performed, which corresponds to a decrease in the peak intensity of TAIm[4-nitrophenolate] at 420 nm and an increase in the peak intensity of TAIm[4-aminophenolate] at 318 nm. At the first 5 min of the reaction, the peak intensity of 4-NP for both NPs in the presence of TAIm[BH_4] IL was drastically reduced. Therefore, $Ag@BH_4^-$ and $Fe_3O_4@BH_4^-$ NPs in the presence of TAIm[BH_4] IL have induction time in seconds. Figure 5B shows the electronic spectra of 4-NP reduction in the absence of TAIm[BH_4] IL and also under ultrasonic conditions. As shown in Fig. 5B, the electronic spectra of 4-NP to 4-AP reduction in the absence of TAIm[BH_4] IL were quite different from when the reduction takes place in the presence of the IL and demonstrated the effect of the IL in the reduction of 4-NP.

The absorption intensity of 4-NP was sharply reduced at 410 nm, but was still visible in the electronic spectrum in the absence of ionic liquid, indicating the effect of the NPs surface properties on the formation of 4-nitrophenolate species. The presence of this peak was another confirmation of the functionalization of NPs with BH_4 groups. Due to the high surface-to-volume ratio of the NPs, 4-nitrorphenolate species were well formed on the surface of the NPs, but nevertheless, in the presence of TAIm[BH_4] IL, the formation of

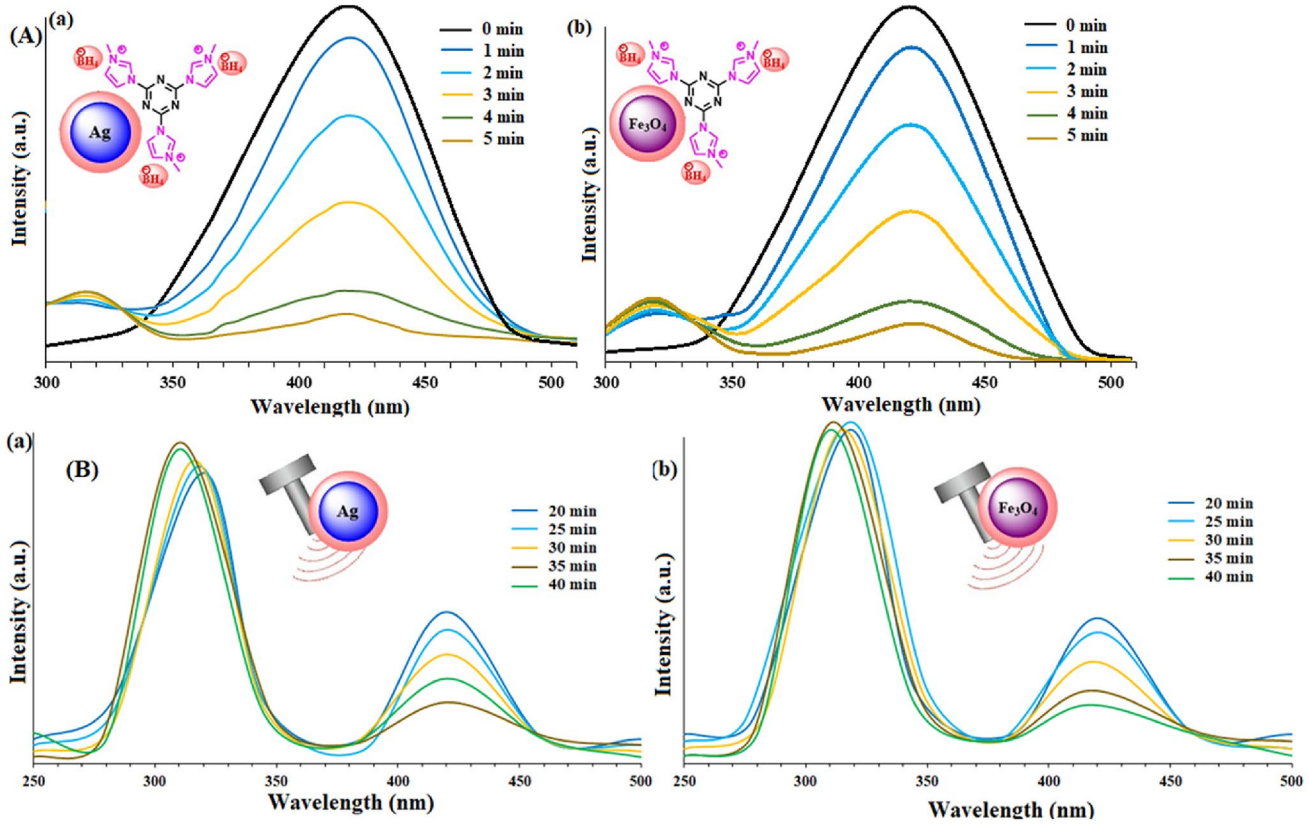

Fig. 5 (A) UV–Vis spectra resulting from the reduction of 4-NP to 4-AP in the presence of TAIm[BH_4] IL catalyzed by **a** Ag@BH_4 NPs and **b** Fe_3O_4@BH_4 NPs. (B) UV–Vis spectra resulting from the reduction of 4-NP to 4-AP in the absence of TAIm[BH_4] IL and under ultrasound irradiation catalyzed by **a** Ag@BH_4 NPs and **b** Fe_3O_4@BH_4 NPs

TAIm[Ph-O] species were more stable. However, over time, the intensity associated with this peak decreases steadily, which corresponds to a decrease in the zeta potential of the nanoparticle surface (Fig. 6). Remarkably, the visible blue shift of the absorption was related to 4-NP at 320 nm to 4-AP at 310 over time, which well illustrates the reduction of 4-NP to 4-AP.

Measurement of zeta potential during 4-NP reduction in the presence of TAIm[BH_4] IL showed that in the first 5 min, the zeta potential for the NPs shifts to more negative values (– 44 mV for Ag@BH_4^- and – 59 mV for Fe_3O_4@BH_4^- NPs) (Fig. 6a). Compared to 4-NP reduction in the absence of TAIm[BH_4] IL (under ultrasonic conditions), this reduction in zeta potential occurs 20 min after the reaction. The results show that the presence of TAIm[BH_4] IL causes better penetration/diffusion of 4-nitrophenlate anion on the surface of the NPs and a significant reduction in induction time. In the absence of TAIm[BH_4] IL, as mechanistic studies will show (also in accordance with the results of characterization analyzes), the IL has a dual function in 4-NP reduction: (1) Due to the capping property of TAIm[BH_4] IL, the NPs were better dispersed in this solvent and consequently the available surface area for 4-NP anion adsorption and reduction reaction was increased (increase of active sites); (2) 4-Nitrophenolate anion can be stabilized by TAIm[BH_4] IL and due to the compatibility of the chemical composition of the nanoparticle surface with TAIm[BH_4] IL, it facilitates the penetration/diffusion and transfer of 4-nitrophenlate anion on the NPs surface. In addition, the TAIm[BH_4] IL also helps to hydrogenate the surface of the NPs during the 4-NP reduction process [66].

For these reasons, in the absence of TAIm[BH_4] IL, the induction time was about 20 min (Fig. 6b), while in the presence of TAIm[BH_4] IL, the induction time was about 2–3 min. The results showed that Ag@BH_4^- NPs had better performance for 4-NP reduction than Fe_3O_4@BH_4^- NPs. The results were completely correlated with the observations obtained from the NPs characterization. The smaller size of Fe_3O_4@BH_4^- NPs, although it provides a larger surface area and a more negative zeta potential for the NPs, but this large surface area creates a larger electrical double layer (caused by the TAIm[BH_4] IL) during preparing the nanoparticles (in agreement with the thermal behavior of the NPs with more weight loss% for Fe_3O_4@BH_4^- NPs) which in turn reduces the analyte access to the catalytic active centers. Another effective factor was the nature of the NPs, which has a direct

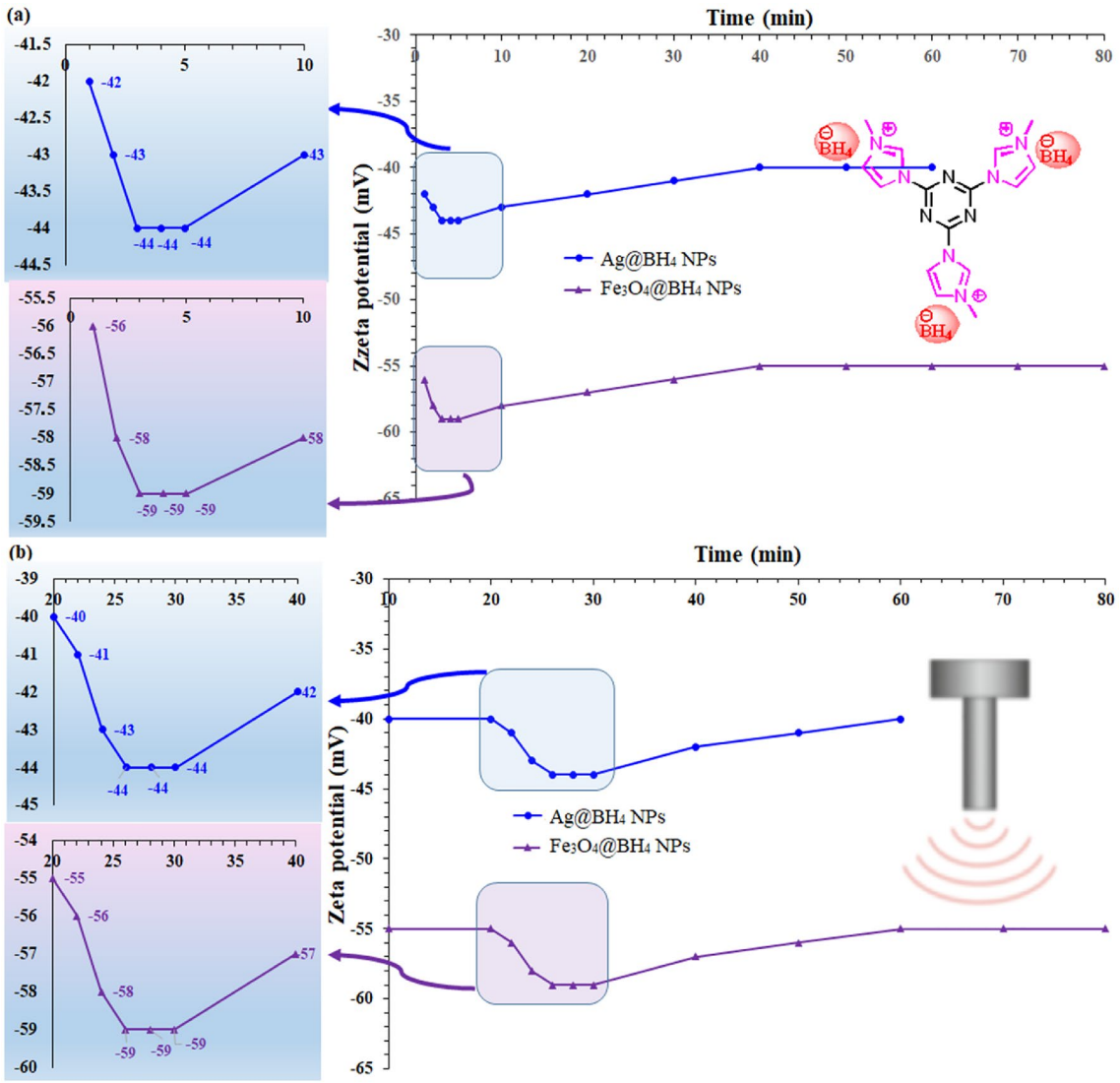

Fig. 6 Zeta potential measurements of $Ag@BH_4^-$ and $Fe_3O_4@BH_4^-$ NPs during reduction of 4-NP **a** in the presence of TAIm[BH_4] IL and **b** in the absence of TAIm[BH_4] IL (under ultrasound irradiation). The left images represent the expand area between **a** 1–10 min and **b** 20–30 min of the 4-NP reduction

relationship with the catalytic properties. Ag NPs are widely known for reducing nitroarenes [66], while Fe_3O_4 NPs lack significant catalytic properties in most cases [16, 43], and are used more as a magnetic core (for easy recovery) and functionalized with molecules and catalytic elements. In this paper, it was shown that the catalytic nanoparticles can be prepared with active molecules such as TAIm[BH_4] IL and used as a catalyst.

3.3 Kinetic studies

The reduction kinetics of 4-NP were studied by $Ag@BH_4^-$ and $Fe_3O_4@BH_4^-$ NPs in the presence or absence of TAIm[BH_4] IL at different time intervals, taking into account induction times of 0 and 20 min, respectively. Due to the fact that TAIm[BH_4] IL was used as a solvent, its concentration was considered constant. The absorption wavelengths for $Ag@BH_4^-$ and $Fe_3O_4@BH_4^-$ NPs were 430 and 250 nm, respectively (Figure S5). The peak at 430 nm was assigned to the surface plasmon resonance (SPR) band for $Ag@BH_4^-$ NPs in agreement with the literature (Figure S5) [1, 67]. According to the obtained results, 4-NP reduction in the presence of $Ag@BH_4^-$ and $Fe_3O_4@BH_4^-$ NPs follows the first-order kinetics, which was in full agreement with the previous reports [68–70]. The catalytic rate constant (k) for the reduction reactions was calculated by Eq. 6:

$$Ln(\frac{A}{A_0}) = -kt \quad (6)$$

where A_0 is the initial absorbance of 4-NP, A is the absorption of 4-NP at time t (sec.), and k is a constant. Figure 7 represents the kinetic curves for the reduction of 4-NP at 430 nm. As shown in Fig. 7, the reaction rate for the reduction of 4-NP in the presence of TAIm[BH_4] IL catalyzed by Ag@BH_4^- and Fe_3O_4@BH_4^- NPs was found to be as (6.75×10^{-3} s^{-1}) and (5.6×10^{-3} s^{-1}), respectively, also, in the absence of TAIm[BH_4] IL they were found as (0.7×10^{-3} s^{-1}) and (0.6×10^{-3} s^{-1}), respectively. As expected and in agreement with the previous observations, the reaction in the presence of TAIm[BH_4] IL was much faster when the reaction was performed in the absence of the IL. Also, the 4-NP reduction rate for Ag@BH_4^- NPs was faster than Fe_3O_4@BH_4^- NPs.

3.4 Control experiments

Two control experiments were designed and accomplished to evaluate the unique activity of Ag@BH_4^- and Fe_3O_4@BH_4^- NPs toward the reduction of 1.0 mmol of 4-NP (Table 5). The previous results have clearly shown that the TAIm[BH_4] IL-mediated synthesized of NPs have the reductive properties toward 4-NP even in the absence of any reducing agent. The results reflect the capping and stabilizing effect of TAIm[BH_4] IL on the NPs synthesis, which the TAIm[BH_4] IL was deposited as a shell on the NPs surface through ionic interactions. No reductive activity was observed for the TAIm[BH_4] IL under normal conditions, as

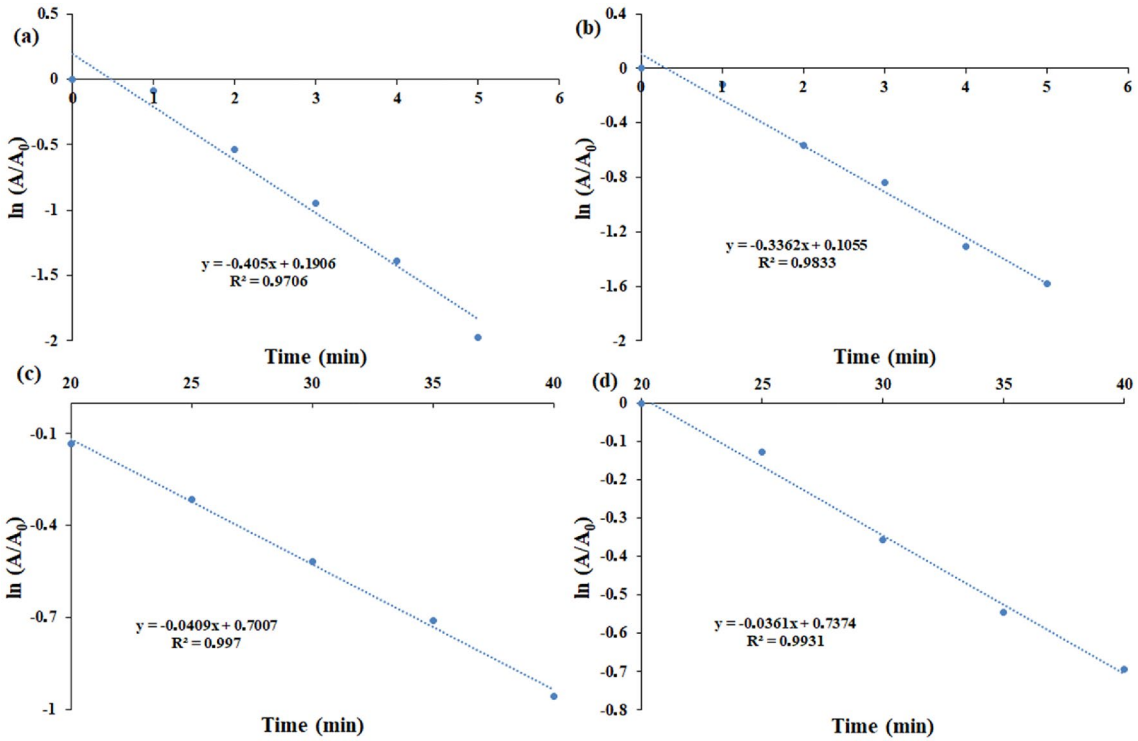

Fig. 7 Plots of ln(A/A_0) versus time (in min) for the reduction of 4-NP to 4-AP in the presence of TAIm[BH_4] IL catalyzed by **a** Ag@BH_4 NPs and **b** Fe_3O_4@BH_4 NPs (t_0=0 min), and in the absence of TAIm[BH_4] IL under ultrasound irradiation catalyzed by **c** Ag@BH_4 NPs, and **d** Fe_3O_4@BH_4 NPs (t_0=20 min)

Table 5 Investigation of catalytic activity of TAIm[I] IL and $NaBH_4$ toward the reduction of 1.0 mmol of 4-NP to 4-AP

Entry	Catalyst	Solvent	Temp. (°C)	Conditions	Time (min)	Conversion (%)[b]
1	–	TAIm[BH_4]	120	Ult. or not[c]	120	0
2	$NaBH_4$	H_2O	120	Ult. or not[c]	120	0

[a]Reaction conditions: 4-NP (1.0 mmol). Catalyst amount: Ag@BH_4^- (5.0 mg), Fe_3O_4@BH_4^- (10.0 mg). Solvent: 2.0 mL. [b]Based on GC. [c]There was not any difference under Ult. and normal conditions

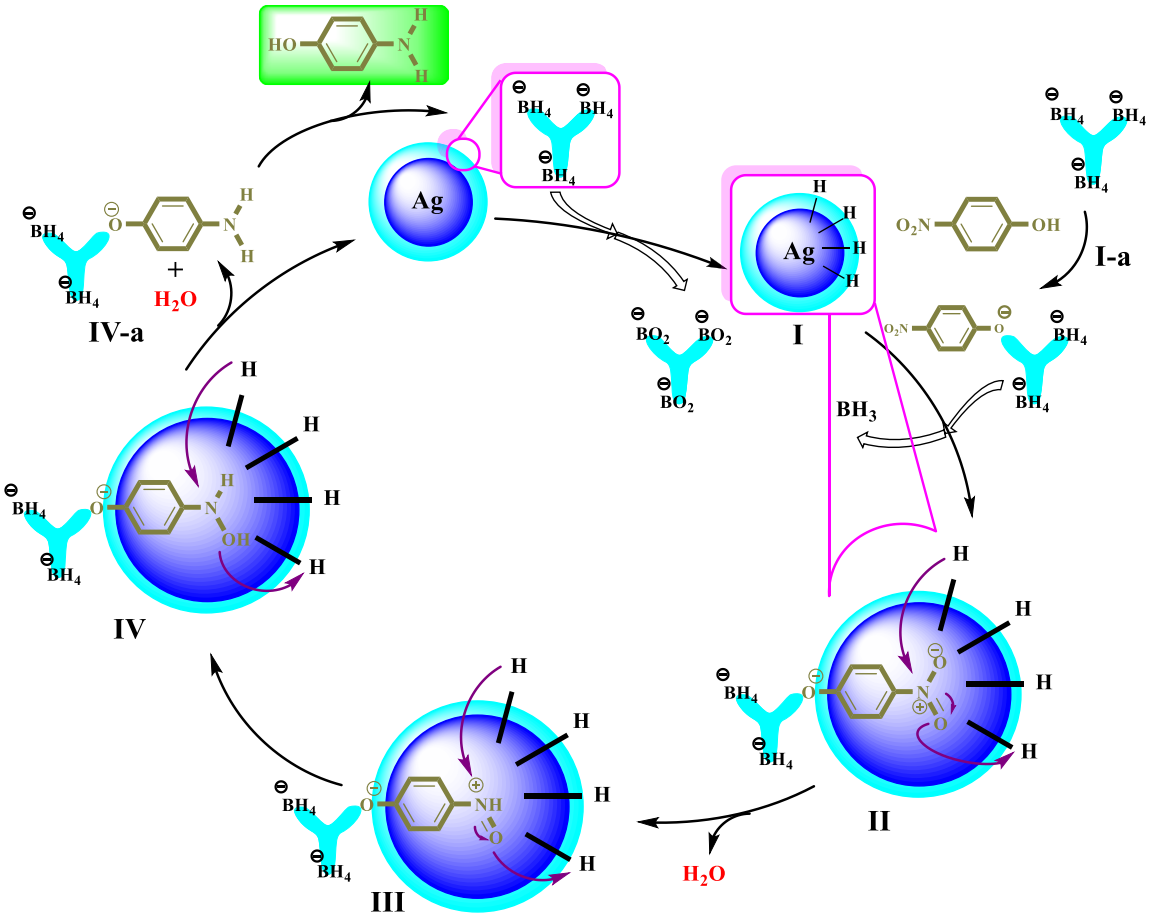

Scheme 3 A plausible reaction mechanism for the reduction of 4-NP catalyzed by $Ag@BH_4^-$ NPs in the presence of TAIm[BH_4] reductive IL. This mechanism could be generalized for $Fe_3O_4@BH_4^-$ NPs

well as $NaBH_4$ (even under ultrasonic irradiation), indicating the vital catalytic effect of the NPs on 4-NP reduction under these conditions (Table 5, entries 3 and 4).

3.5 Mechanism studies

The results of optimization experiments as well as control tests showed that $Ag@BH_4^-$ and $Fe_3O_4@BH_4^-$ NPs can also reduce 4-NP to 4-AP in the absence of a reducing agent. Considering the proof of capping capability of TAIm[BH_4] IL and also the reduction of 4-NP in the absence of the IL, it seems that the formation of $Ag@BH_4^-$ and $Fe_3O_4@BH_4^-$ NPs undergoes proton adsorption on their surfaces in the presence of TAIm[BH_4] IL. Scheme 3 shows the reduction mechanism of 4-NP in the presence of $Ag@BH_4^-$ NPs, which can also be generalized to $Fe_3O_4@BH_4^-$ NPs. As shown in Scheme 3, the BH_4 groups in TAIm[BH_4] IL were converted to the TAIm[BO_2] groups [71, 72] in the presence of Ag NPs and cause the adsorption of protons on the nanoparticles surface (Stage I). This phenomenon can also occur during the preparation of nanoparticles and was responsible for the observed catalytic activity of NPs in the absence of a reducing agent. Ultrasonic waves cause 4-NP to penetrate/diffuse to the surface of nanoparticles and pass through the electrical double layer (stage II) [73]. According to the results shown in Table 3 (entries 1–4), $Ag@BH_4^-$ and $Fe_3O_4@BH_4^-$ NPs have very low efficiency in the absence of ultrasonic in water solvent. The next effective factor was the possibility of stability of 4-nitrophenolate ion by TAIm[BH_4] IL and formation of TAIm[4-nitrophenolate] groups, which can easily penetrate/diffuse to the surface of NPs and reduce 4-NP to 4-AP (Scheme 3). Step I-a shows the immobilization of 4-NP via the phenolic group on the TAIm[BH_4] IL with the formation of BH_3^- groups. The explanation given was completely consistent with the results of the reduction of 4-NP in TAIm[BH_4] IL (Table 3, entries 5 and 6) compared to when the reaction was performed in water (Table 3, entries 1–4). After several steps of hydrogen transfer from the surface of nanoparticles to the nitro group of 4-NP (steps II, III, IV), intermediate IV-a is formed. Eventually, upon receiving a proton from

the medium, 4-aminophenoxide is converted to 4-AP product, and the ionic liquid returns to the cycle.

The structure of the ionic liquids includes the counter anion as a reducing agent and a cation core, including the imidazolium groups, is responsible for the observed stability and capping role for the nanoparticles formation. Ag (or Fe) ions are reduced by borohydride groups in the ionic liquid, and the cationic part (imidazolium part of the ionic liquid) forms a monolayer on the surface of the nanoparticles [28, 35, 36, 74]. This coating not only prevents the agglomeration of nanoparticles by increasing the positive charges on the surface of the nanoparticle, but also changes the value of the zeta potential on the surface of the nanoparticle, which is defined as the potential difference between the surface of the nanoparticle dispersed in a conductive liquid and the bulk of the liquid [75].

3.6 Determination of antioxidant capacities of ionic liquids and NPs

Antiradical activity of the IL and NPs was measured by DPPH assay. The methanolic solution of DPPH has a purple color with an absorption at λ_{max} = 516–520 nm, that after reduction in the presence of an antioxidant, the absorption shifted to 400 nm [76]. Therefore, measure of the reduction in the absorption intensity of DPPH in the presence of an antioxidant corresponds to the antioxidant capacity of the reagent. Figure 8 shows the antioxidant activity of the NPs as well as the IL as a function of concentration. Standard ascorbic acid was used as a positive control [77]. The most antiradical activity was observed for $Ag@BH_4^-$ NPs, where DPPH radicals were quenched at 100 µg/mL concentration of the NPs, higher than ascorbic acid activity as a standard antioxidant (Fig. 8). The results also showed a linear relationship between the NPs/ILs concentration and inhibition percentage in agreement with the literature [78, 79]. Next, $Fe_3O_4@BH_4^-$ NPs also showed high antiradical activity, which the total DPPH quenching was observed at 180 µg/mL.

Remarkably, the high antioxidant activity of $Fe_3O_4@BH_4^-$ and $Ag@BH_4^-$ NPs was at very low concentrations of 10 µg/mL, so that IC_{50} for the NPs occurs at lower concentrations. TAIm[BH_4] IL showed a 70% inhibitory effect at a concentration of 200 µg/mL, which reflects its remarkable antioxidant capacity. Insignificant antioxidant activity was observed for TAIm[I] IL even at higher concentrations, which in comparison with TAIm[BH_4] IL, indicated the reducing effect of BH_4 counter ion in agreement with the reduction of Fe and Ag ions.

3.7 Recyclability and stability of NPs

Nanoparticles recyclability was evaluated for 4-NP reduction. In order to study the stability of the NPs under ultrasonic conditions, this study was also performed in this conditions. After each cycle of recovery, the NPs were separated from the reaction mixture by centrifugation (or by applying an external magnet in the case of $Fe_3O_4@BH_4$) and injected into the GC apparatus. Significantly, there was a significant decrease in 4-NP reduction efficiency in the absence of TAIm[BH_4] IL (under ultrasonic waves) during successive recovery cycles. As shown in Fig. 9, no significant decrease was observed for the both nanoparticles in the presence of TAIm[BH_4] IL for 4-NP reduction during 10 consecutive

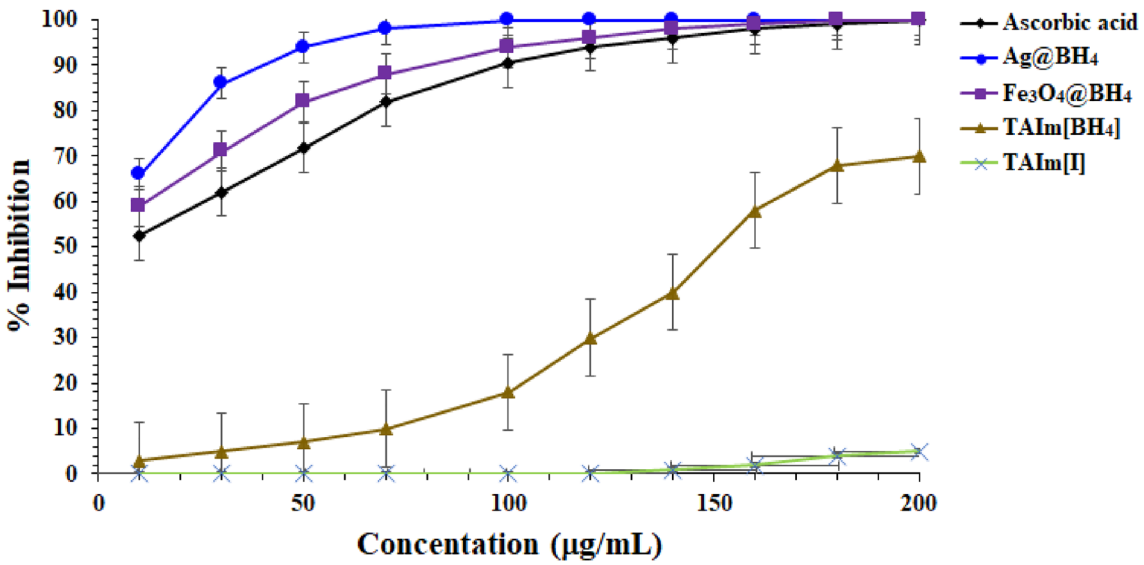

Fig. 8 DPPH radical scavenging of the NPs as well as ILs at various concentrations

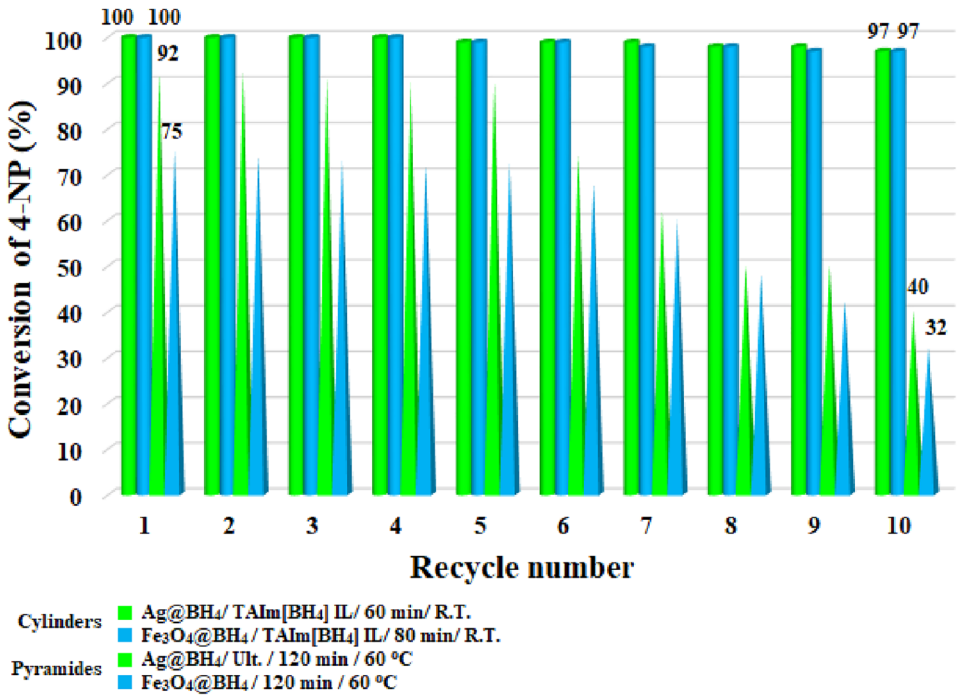

Fig. 9 Recycling studies of $Fe_3O_4@BH_4^-$ and $Ag@BH_4.^-$ NPs over 4-NP reduction in the presence of $TAIm[BH_4]$ IL and Ult. conditions (in the absence of $TAIm[BH_4]$ IL)

cycles, whereas, in the absence of $TAIm[BH_4]$ IL, from the fifth cycle onward, the 4-NP %conversion for $Ag@BH_4^-$ and $Fe_3O_4@BH_4^-$ NPs decreased to 90% and 72%, respectively, and reached 40% and 32% at the end of the tenth cycle. TEM images from the recovered NPs (under ultrasonic conditions) showed that the NPs retained their morphology and this decrease in efficiency was due to changes in the surface properties of the NPs during successive reduction cycles (Fig. 10). The $TAIm[BH_4]$ IL maintains the catalytic activity as well as the surface properties of the nanoparticles; In other words, the $TAIm[BH_4]$ IL reactivates the NPs in each cycle. For this purpose, EDX analysis was performed

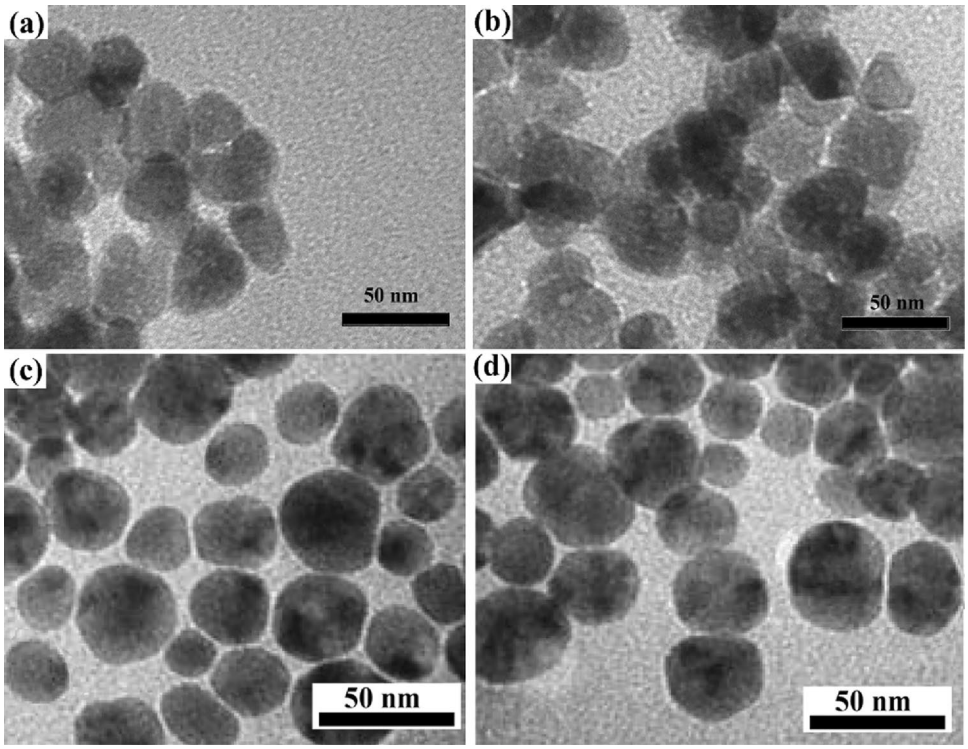

Fig. 10 TEM images of the recycled NPs after 10th run. **a** $Fe_3O_4@BH_4^-$ and **c** $Ag@BH_4^-$ NPs under Ult. conditions. **b**, **d** $Fe_3O_4@BH_4$ and **c** $Ag@BH_4$ NPs in the presence of $TAIm[BH_4]$ IL

on the recovered NPs at different recycles. As shown in Table 6, the percentage of oxygen in successive cycles for the both nanoparticles increased and the percentage of B element decreased. According to the proposed mechanism, the results were completely consistent with the formation of BO_2 groups by 4-NP reduction on the surface of NPs during consecutive cycles. Reduction of 4-NP in the presence of TAIm[BH_4] IL catalyzed by Ag@BH_4^- and Fe_3O_4@BH_4^- NPs did not cause any significant change until the tenth cycle in the elemental percentage composition of the NPs (Table 6). The results also showed that the magnetic properties of Fe_3O_4@BH_4^- NPs remain completely intact during consecutive cycles and the NPs do not suffer any drop in magnetic properties even after the tenth cycle.

In addition, the results demonstrated a high short-term and long-term stability for the NPs. For this purpose, their electronic spectra, zeta potentials, and the mean diameters (by DLS analysis) were studied and determined at different time intervals, which provide a good estimate for the stability of the NPs. Figure S6 shows the electronic spectra of the nanoparticle after 20, 40, 60, and 80 days of preparation. As shown in Figure S6a, no peak shift for the SPR band of Ag@BH_4^- NPs at 430 nm was observed over time and only its absorption intensity decreases [80, 81]. Also, no change in the electronic absorption of Fe_3O_4@BH_4^- NPs was observed, which indicates their stability over time (Figure S6b). The non-change of the electronic spectra of the NPs confirms the non-change of morphology and deviation from the spherical state, as well as their non-agglomeration, so that they can be kept for a long time [82]. DLS and zeta analyses for the NPs were also studied at different time intervals (inset Tables in Fig. S6). According to the results, the average size of Ag@BH_4^- NPs showed an increase of only 2 nm in the period of 80 days, which reflects the insignificant agglomeration of the NPs. The zeta potential also decreased from -40 mV in the freshly prepared Ag@BH_4^- to – 36 after 80 days. No visible change in the diameter of Fe_3O_4@BH_4^- NPs was observed even after 80 days (Fig. S6b, inset table). In addition, the zeta potential of Fe_3O_4@BH_4^- NPs also remained constant during this period.

3.8 Comparison of the catalytic activity of the NPs with previously reported ones

In the end, the catalytic activity of Fe_3O_4@BH_4 and Ag@BH_4 NPs was compared and investigated with previously reported catalytic systems based on Ag and Fe_3O_4 in order to reduce 4-NP to 4-AP. Also, Liao et al. compared the catalytic activity of a wide range of polymer-supported Ag NPs catalysts, carbon-supported Ag NPs catalysts, oxides-supported Ag NPs catalysts, MOFs-supported Ag NPs and porous organic frameworks (POFs)-supported Ag NPs catalysts, anisotropic Ag NPs catalysts, bimetallic Ag NPs catalysts in a review paper [65].

Table 7 shows this comparison from the point of view of the conditions used for the reduction of 4-NP, nanoparticle recovery capability, reducing agent, reaction rate constant, and antioxidant activity toward DPPH. As shown in Table 7, and also in agreement with the extensive comparisons made by Liao et al. [65], the prepared Fe_3O_4@BH_4 and Ag@BH_4 NPs have advantages such as long-term stability without degradation or agglomeration, high antioxidant properties, and does not require functionalization, making it superior to many catalytic systems based on silver and magnetite nanoparticles. As shown in Table 7, most of the catalytic systems based on Ag NPs (and especially magnetite NPs) need to be functionalized with various compounds through tedious reactions, which is not only cost-effective, but also changes the surface characteristics and morphology of the NPs. Several reports have shown that naked magnetite nanoparticles

Table 6 EDX analyses of recycled Fe_3O_4@BH_4 and Ag@BH_4 NPs over 4-NP reduction in two different conditions described in Table 3

NPs	Conditions	Run	EDX analysis (%wt)						Mgn. (emu/g)
			B	C	N	O	Fe	Ag	
Fe_3O_4@BH_4^-	60 °C/Ult./120 min	1	3.21	15.05	9.42	9.12	63.20	–	62.0
		5	2.82	14.78	9.20	10.16	63.04	–	62.0
		10	2.12	13.68	9.20	12.89	63.11	–	61.95
Ag@BH_4^-	60 °C/Ult./120 min	1	3.34	19.81	12.11	1.54	–	63.20	–
		5	3.08	19.92	12.08	1.80	–	63.12	–
		10	2.80	19.76	12.13	2.22	–	63.09	–
Fe_3O_4@BH_4^-	TAIm[BH_4]/ R.T./80 min	1	3.11	14.55	9.46	9.16	63.72	–	62.0
		5	3.22	14.50	9.44	9.10	63.74	–	62.0
		10	3.20	14.52	9.49	9.09	63.70	–	62.0
Ag@BH_4^-	TAIm[BH_4]/R.T./60 min	1	3.34	19.80	12.12	1.54	–	63.20	–
		5	3.36	19.76	12.20	1.50	–	63.18	–
		10	3.38	19.79	12.08	1.56	–	63.18	–

Table 7 Comparison of catalytic activity for various Ag-based NPs catalysts toward 4-NP reduction to 4-AP

Entry	Catalyst	Conditions	Mol%[a]	Reducing agent	Rec./NOR[b]	K (s^{-1})	IC_{50} (μg/ml)[c]	[Ref.]
1	Ag@CTGU-3[d]	S.F./R.T	–[e]	KBH_4	Yes/3	8.64 (s^{-1} g^{-1})	N.A	[83]
2	Fe_3O_4@SN/HPW@CG–Ag[f]	H_2O /R.T	0.2	$NaBH_4$	Yes/10	5.5×10^{-3}	N.A	[84]
3	CNFs/AgNPs[g]	H_2O /25 °C	–[e]	$NaBH_4$	Yes/–	4.6×10^{-3}	N.A	[85]
4	$RhAg_{0.5}$/rGO	H_2O, 20 °C	0.2	$NaBH_4$	Yes/5	14.8×10^{-3}	N.A	[86]
5	Ag@CAF[h]	H_2O/R.T	4.9	$NaBH_4$	Yes/5	2.9×10^{-3}	N.A	[87]
6	$Ag@TiO_2$	H_2O/R.T	4.6	$NaBH_4$	Yes/5	1.8×10^{-3}	N.A	[87]
7	GSH-AgNPs[i]	H_2O/25 °C	–[e]	$NaBH_4$	No	0.03×10^{-3}	N.A	[88]
8	Ag/N–C[j]	H_2O/R.T	485	$NaBH_4$	Yes/7	2×10^{-3}	N.A	[89]
9	PS@PAMAM-Ag	H_2O/25 °C	12.5	$NaBH_4$	Yes/–	0.84×10^{-3}		
10	$Fe_3O_4@BH_4^-$	TAIm[BH_4]/RT	–	–	Yes/10	5.6×10^{-3}	< 10	This work
11	$Ag@BH_4^-$	TAIm[BH_4]/R.T	2.93	–	Yes/10	6.7×10^{-3}	< 10	This work

[a]Based on Ag mmols. [b]Number of recycling. [c]Against DPPH free radicals. [d]$[Zn_5(\mu_3\text{-}H_2O)_2(L1)_2]\cdot3DMA\cdot4H_2O$ (Ag NPs embedded in Zn3/Zn5-cluster-based metal–organic frameworks). [e] Impossibility of calculation due to insufficient information.[f] *SN* saline, *HPW* phosphotungstic acid, *CG* chitosan. [g]*CNFs* carbon nanofibers. [h]*CAF* cellulose acetate filter paper. [i]Glutathione. [j]N-doped carbon

(without functionalization) lack any significant catalytic or antioxidant activity [17, 18], while $Fe_3O_4@BH_4^-$ and $Ag@BH_4^-$ NPs showed a significant antioxidant activity ($IC_{50} < 10$ μg/mL), which was higher than the antioxidant activity of magnetite NPs functionalized by tedious methods.

Another advantage of the catalytic systems presented in this work was not using a reducing agent for the reduction reactions. This advantage causes the reaction environment to be cleaner, and the purification of the products is done easily (easy work-up). TAIm[BH_4] IL was not only used as a solvent to reduce 4-NP to 4-AP, but also used as an effective reducing agent for the reduction of these compounds. In addition, $Ag@BH_4^-$ NPs were prepared by TAIm[BH_4] IL in the absence of any surfactant and capping agent, which was not only cost-effective, but also environmentally friendly. The results of this study also showed that magnetite NPs can be well prepared by TAIm[BH_4] IL as a reducing and capping agent.

4 Conclusion

In conclusion, $Ag@BH_4^-$ and $Fe_3O_4@BH_4^-$ NPs were synthesized using reductive TAIm[BH_4] IL in one step and the resulting $Fe_3O_4@BH_4^-$ and $Ag@BH_4^-$ catalytic NPs were served for the selective reduction of 4-NP to 4-AP. The NPs were characterized by TEM, HRTEM, UV–Vis, TGA, VSM, XRD, EDX, XPS, and DLS analyses. TAIm[BH_4] IL acts not only as a reducing agent and solvent for Ag and Fe ions, but also plays the role of a capping agent and prevents the agglomeration of nanoparticles. The reduction also could be performed in the absence of IL in water under ultrasound waves catalyzed by the NPs. The NPs follows first-order kinetics for the reduction of 4-NP. The reaction rates in the presence of TAIm[BH_4] IL catalyzed by $Ag@BH_4^-$ and $Fe_3O_4@BH_4^-$ NPs were found to be 6.75 ($\times10^{-3}$ s^{-1}) and 5.6 ($\times10^{-3}$ s^{-1}), respectively. High antioxidant activity was found for $Fe_3O_4@BH_4^-$ and $Ag@BH_4^-$ NPs at very low concentrations of 10 μg/mL, so that IC_{50} for nanoparticles occurs at lower concentrations. Also, TAIm[BH_4] IL showed 70% inhibitory effect at a concentration of 200 μg/mL. The NPs could be recycled for at least ten consecutive recycles with insignificant loss of catalytic activity in the presence of TAIm[BH_4] IL that was confirmed by TEM and EDX analyses. TAIm[BH_4] IL was prepared via a simple route from cheap and accessible reactants, which could be served as a reducing agent and capping agent toward the preparation of a variety of metal nanoparticles via the reduction of the corresponding metal ions.

Supplementary Information The online version contains supplementary material available at https://doi.org/10.1007/s00339-022-06154-z.

Acknowledgements The authors are grateful to the Golestan University for their financial support.

Declarations

Conflict of interest The authors declare that they have no conflict of interest.

References

1. M. Nanaei, M.A. Nasseri, A. Allahresani, M. Kazemnejadi, Appl. Sci. **1**, 1 (2019)
2. D. Xu, M. Xiong, M. Kazemnejadi, RSC Adv. **11**, 12484 (2021)
3. T. Chen, Z. Liu, K. Zhang, B. Su, Z. Hu, H. Wan, Y. Chen, X. Fu, Z. Gao, A.C.S. Appl, Mater. Interfaces **13**, 50539 (2021)
4. L. Mulfinger, S.D. Solomon, M. Bahadory, A.V. Jeyarajasingam, S.A. Rutkowsky, C. Boritz, J. Chem. Educ. **84**, 322 (2007)

5. S. Dawadi, S. Katuwal, A. Gupta, U. Lamichhane, R. Thapa, S. Jaisi, G. Lamichhane, D.P. Bhattarai, N. Parajuli, J. Nanomater. **2021**, 6687290 (2021)
6. A. Pal, S. Shah, S. Devi, Mater. Chem. Phys. **114**, 530 (2009)
7. K. Mavani, M. Shah, Int. J. Eng. Res. Technol. **2**, 1 (2013)
8. J. Kasthuri, S. Veerapandian, N. Rajendiran, Colloids Surf. B **68**, 55 (2009)
9. K. Ponsanti, B. Tangnorawich, N. Ngernyuang, C. Pechyen, J. Mat. Res. Technol. **9**, 11003 (2020)
10. R. Shankar, L. Groven, A. Amert, K.W. Whites, J.J. Kellar, J. Mater. Chem. **21**, 10871 (2011)
11. M. Khan, F. Ahmad, J.T. Koivisto, M. Kellomäki, Colloid Interface. Sci. Commun. **39**, 100322 (2020)
12. H. Salehizadeh, E. Hekmatian, M. Sadeghi, K. Kennedy. J. Nanobiotechnol. **10**, 1 (2012)
13. A.A. Gadgeel, S.T. Mhaske, C. Duerr, K.L. Liu, J. Inorg. Organomet. Polym. Mater. **29**, 1688 (2019)
14. S.V. Salihov, Y.A. Ivanenkov, S.P. Krechetov, M.S. Veselov, N.V. Sviridenkova, A.G. Savchenko, N.L. Klyachko, Y.I. Golovin, N.V. Chufarova, E.K. Beloglazkina, A.G. Majouga, J. Magn. Magn. Mater. **394**, 173 (2015)
15. W. Zhang, F. Shen, R. Hong, Particuology **9**, 179 (2011)
16. M. Kazemnejadi, M.A. Nasseri, S. Sheikh, Z. Rezazadeh, S.A. Alavi, RSC Adv. **11**, 15989 (2021)
17. S. Verma, S. Kujur, R. Sharma, D.D. Pathak, ACS Omega **7**, 9754 (2022)
18. M. Li, Z. Cui, E. Li, Ceram. Int. **45**, 14449 (2019)
19. L. Zhang, Z. Cui, Front. Chem. **10**, 898174 (2022)
20. S. Goktas, A. Goktas, J. Alloys Compd. **863**, 158734 (2021)
21. L. Zhang, Z. Cui, Nanomaterials **12**, 1712 (2022)
22. B. Karimi, M. Tavakolian, M. Akbari, F. Mansouri, Chem. Cat. Chem **10**, 3173 (2018)
23. X. Wang, M. Salari, D.E. Jiang, J.C. Varela, B. Anasori, D.J. Wesolowski, S. Dai, M.W. Grinstaff, Y. Gogotsi, Nat. Rev. Mater. **5**, 787 (2020)
24. R. Martínez-Palou, J. Mex. Chem. Soc. **51**, 252 (2007)
25. D.C. Murador, A.R.C. Braga, P.L. Martins, A.Z. Mercadante, V.V. de Rosso, Food Res. Int. **126**, 108653 (2019)
26. M. Hejazifar, O. Lanaridi, K. Bica-Schröder, J. Mol. Liq. **303**, 112264 (2020)
27. M.M. Seitkalieva, D.E. Samoylenko, K.A. Lotsman, K.S. Rodygin, V.P. Ananikov, Coord. Chem. Rev. **445**, 213982 (2021)
28. J. Łuczak, M. Paszkiewicz, A. Krukowska, A. Malankowska, A. Zaleska-Medynska, Adv. Colloid Interface Sci. **227**, 1 (2016)
29. E. Avirdi, S.E. Hooshmand, H. Sepahvand, V. Vishwanathan, I. Bahadur, L.M. Katata-Seru, R.S. Varma, Ionic liquids-assisted greener preparation of silver nanoparticles. Curr. Opin. Green Sustain. Chem **33**, 100581 (2021)
30. M.I. Qadir, A. Kauling, L. Calabria, T. Grehl, J. Dupont, Nano Struct. Nano Objects **14**, 92 (2018)
31. H. Er, H. Yasuda, M. Harada, E. Taguchi, M. Iida, Colloids Surf. A **522**, 503 (2017)
32. U.S. Shin, H.K. Hong, H.W. Kim, M.S. Gong, Bull. Korean Chem. Soc. **32**, 1583 (2011)
33. N. Tian, X. Ni, Z. Shen, React. Funct. Polym. **101**, 39 (2016)
34. W. Darwich, C. Gedig, H. Srour, C.C. Santini, M.H. Prechtl, RSC Adv. **3**, 20324 (2013)
35. E. Husanu, C. Chiappe, A. Bernardini, V. Cappello, M. Gemmi, Colloids Surf. A **538**, 506 (2018)
36. A. Gholami, M.S. Shams, A. Abbaszadegan, M. Nabavizadeh, Green Process Synth. **10**, 585 (2021)
37. V. Patil, S. Mahajan, M. Kulkarni, K. Patil, C. Rode, A. Coronas, G.R. Yi, Chemosphere **243**, 125302 (2020)
38. D. Dorjnamjin, M. Ariunaa, Y.K. Shim, Int. J. Mol. Sci. **9**, 807 (2008)
39. Y. Zhu, G. Xu, M. Kazemnejadi, New J. Chem. **45**, 11662 (2021)
40. Y. Hu, M. Ren, M. Kazemnejadi, ChemistryOpen **10**, 775 (2021)
41. Q. Min, P. Miao, D. Chu, J. Liu, M. Qi, M. Kazemnejadi, Catal. Lett. **151**, 3030 (2021)
42. A.R. Sardarian, M. Kazemnejadi, M. Esmaeilpour, Dalton Trans. **48**, 3132 (2019)
43. A.R. Sardarian, M. Kazemnejadi, M. Esmaeilpour, Appl. Organomet. Chem. **35**, e6051 (2021)
44. M. Esmaeilpour, J. Javidi, J. Chin. Chem. Soc. **62**, 328 (2015)
45. Z. Sharafi, J. Ranjbari, J. Javidi, N. Nafissi-Varcheh, M. Tabarzad, Trends Pept. Protein Sci. **1**, 20 (2016)
46. A. Das, M.T. Prabhu, N. Sarkar, Adv. Nat. Sci. Nanosci. Nanotechnol. **13**, 015002 (2022)
47. M. Mani, M.K. Okla, S. Selvaraj, A.R. Kumar, S. Kumaresan, A. Muthukumaran, K. Kaviyarasu, M.A. El-Tayeb, Y.B. Elbadawi, K.S. Almaary, B.M.A. Almunqedhi, Environ. Res. **198**, 111199 (2021)
48. B. Lesiak, N. Rangam, P. Jiricek, I. Gordeev, J. Tóth, L. Kövér, M. Mohai, P. Borowicz, Front. Chem. **7**, 642 (2019)
49. M.A. Nasseri, Z. Rezazadeh, M. Kazemnejadi, A. Allahresani, Dalton Trans. **49**, 10645 (2020)
50. R.S. El-Tawil, S.T. El-Wakeel, A.E. Abdel-Ghany, H.A. Abuzeid, K.A. Selim, A.M. Hashem, Heliyon **5**, e02415 (2019)
51. F. Heidary, D. Ghanbari, Nanochem. Res. **6**, 117 (2021)
52. S. Giuffrida, G. Ventimiglia, S. Sortino, Chem. Commun. (2009). https://doi.org/10.1039/b907075c
53. M. Jouyandeh, S.M.R. Paran, M. Shabanian, S. Ghiyasi, H. Vahabi, M. Badawi, K. Formela, D. Puglia, M.R. Saeb, Prog. Org. Coat. **123**, 10 (2018)
54. Z. Cui, S. Zhang, L. Wang, K. Yang, Micro Nanostruct (2022). https://doi.org/10.1016/j.micrna.2022.207260
55. A. Hashim, Q. Hadi, J. Inorg. Organomet. Polym. Mater. **28**, 1394 (2018)
56. A. Goktas, S. Modanlı, A. Tumbul, A. Kilic, J. Alloys Compd. **893**, 162334 (2022)
57. Y. Chi, Q. Yuan, Y. Li, J. Tu, L. Zhao, N. Li, X. Li, J. Colloid Interface Sci. **383**, 96 (2012)
58. A. Tumbul, F. Aslan, A. Goktas, M.Z. Zarbali, A. Kilic, Mater. Chem. Phys. **258**, 123997 (2021)
59. F. Mikailzade, F. Önal, M. Maksutoglu, M. Zarbali, A. Göktaş, J. Supercond. Novel Magn. **31**, 4141 (2018)
60. A. Hajalilou, L.P. Ferreira, M.M. Jorge, C.P. Reis, M.M. Cruz, J. Magn. Magn. Mater. **537**, 168242 (2021)
61. A. Goktas, Appl. Surf. Sci. **340**, 151 (2015)
62. N.B. Turan, H.S. Erkan, G.O. Engin, M.S. Bilgili, Process Saf. Environ. Prot. **130**, 238 (2019)
63. M. Li, G. Chen, Nanoscale **5**, 11919 (2013)
64. M. Riaz, V. Mutreja, S. Sareen, B. Ahmad, M. Faheem, N. Zahid, G. Jabbour, J. Park, Sci. Rep. **11**, 1 (2021)
65. G. Liao, Y. Gong, L. Zhong, J. Fang, L. Zhang, Z. Xu, H. Gao, B. Fang, Nano Res. **12**, 2407 (2019)
66. P. Li, Y. Wang, H. Huang, S. Ma, H. Yang, Z.L. Xu, Chemosphere **263**, 127995 (2021)
67. M. Akter, M.T. Sikder, M.M. Rahman, A.A. Ullah, K.F.B. Hossain, S. Banik, T. Hosokawa, T. Saito, M. Kurasaki, J. Adv. Res. **9**, 1 (2018)
68. M. Ul-Islam, J. Ali, W. Khan, A. Haider, N. Shah, M.W. Ahmad, M.W. Ullah, G. Yang, Eng. Sci. **8**, 19 (2019)
69. A. Šileikaitė, J. Puišo, I. Prosyčevas, S. Tamulevičius, Mater. Sci. **15**, 21 (2009)
70. R. Grzeschik, D. Schäfer, T. Holtum, S. Küpper, A. Hoffmann, S. Schlücker, J. Phys. Chem. C **124**, 2939 (2020)
71. R. Krishna, D.M. Fernandes, C. Dias, J. Ventura, E.V. Ramana, C. Freire, E. Titus, Int. J. Hydrogen Energy **40**, 4996 (2015)
72. M.I. Din, R. Khalid, Z. Hussain, T. Hussain, A. Mujahid, J. Najeeb, F. Izhar, Crit. Rev. Anal. Chem. **50**, 322 (2020)

73. J.R. Chiou, B.H. Lai, K.C. Hsu, D.H. Chen, J. Hazard Mater. **248**, 394 (2013)
74. C.D. Gu, Y.H. You, Y.L. Yu, S.X. Qu, J.P. Tu, Surf. Coat. Technol. **205**, 4928 (2011)
75. M. Yamamoto, Y. Kashiwagi, M. Nakamoto, Langmuir **22**, 8581 (2006)
76. M.A. Nasseri, S. Behravesh, A. Allahresani, M. Kazemnejadi, Bioresour Bioprocess **6**, 1 (2019)
77. O. Arrigoni, M.C. De Tullio, Biochim. Biophys. Acta Gen. Subj. **1569**, 1 (2002)
78. R.S. Priya, D. Geetha, P.S. Ramesh, Ecotoxicol. Environ. Saf. **134**, 308 (2016)
79. A. Bouafia, S.E. Laouini, A. Khelef, M.L. Tedjani, F. Guemari, J. Cluster. Sci. **32**, 1033 (2021)
80. R.A. Hamouda, M.H. Hussein, R.A. Abo-Elmagd, S.S. Bawazir, Sci. Rep. **9**, 1 (2019)
81. G. Ghodake, M. Kim, J.S. Sung, S. Shinde, J. Yang, K. Hwang, D.Y. Kim, Nanomaterials **10**, 360 (2020)
82. S. Ali, M.R. Shah, S. Hussain, S. Khan, A. Latif, M. Ahmad, M. Ali, J. Cluster Sci. **413**(1), 413–420 (2022)
83. X.Q. Wu, D.D. Huang, Z.H. Zhou, W.W. Dong, Y.P. Wu, J. Zhao, D.S. Li, Q. Zhang, X. Bu, Dalton Trans. **46**, 2430 (2017)
84. Z. Wang, S. Zhai, B. Zhai, Z. Xiao, F. Zhang, Q. An, New J. Chem. **38**, 3999 (2014)
85. P. Zhang, C. Shao, Z. Zhang, M. Zhang, J. Mu, Z. Guo, Y. Liu, Nanoscale **3**, 3357 (2011)
86. C. Wang, R. Ciganda, L. Yate, S. Moya, L. Salmon, J. Ruiz, D. Astruc, J. Mater. Sci. **52**, 9465 (2017)
87. S.M. Albukhari, M. Ismail, K. Akhtar, E.Y. Danish, Colloids Surf. A **577**, 548 (2019)
88. R. Rajamanikandan, K. Shanmugaraj, M. Ilanchelian, J. Cluster Sci. **28**, 1009 (2017)
89. N. Alhokbany, T. Ahama, M. Naushad, S.M. Alshehri, Compos. B **173**, 106950 (2019)

Authors and Affiliations

Saade Abdalkareem Jasim[1] · Usama S. Altimari[2] · Halah T. Mohammed[3] · Mustafa K. Suhayb[4] · Abduladheem Turki Jalil[5] · Milad Kazemnejadi[6]

✉ Saade Abdalkareem Jasim
saade.a.j@uoa.edu.iq

✉ Halah T. Mohammed
halah.thamer@mustaqbal-college.edu.iq

✉ Milad Kazemnejadi
miladkazemnejad@yahoo.com

[1] Al-Maarif University College Medical Laboratory Techniques Department, Al-Anbar-Ramadi, Iraq

[2] Al-Nisour University College, Baghdad, Iraq

[3] Anesthesia Techniques Department, Al-Mustaqbal University College, Babylon, Iraq

[4] Al-Manara College for Medical Sciences, Maysan, Iraq

[5] College of Technical Engineering, The Islamic University, Najaf, Iraq

[6] Department of Chemistry, Faculty of Science, Golestan University, Gorgan, Iran